

ALMA MATER STUDIORUM · UNIVERSITÀ DI BOLOGNA

School of Science
Department of Physics and Astronomy
Master Degree Programme in Astrophysics and Cosmology

High-resolution spectroscopy of metal-poor stars in the Small Magellanic Cloud

Graduation Thesis

Presented by:
Lorenzo Santarelli

Supervisor:
Prof. Alessio Mucciarelli

Academic Year 2023/2024
Graduation date III

Contents

1	Introduction	5
1.1	The metal-poor stars	5
1.2	The Magellanic Clouds	6
1.3	Metal-poor stars in the Magellanic Clouds	7
1.4	The aim of this work	12
2	Spectroscopic Dataset	15
3	Spectroscopic Analysis	19
3.1	Atmospheric parameters	19
3.2	Computation of synthetic spectra	21
3.3	Radial velocities	22
3.4	Line selection	23
3.5	Preliminary analysis with DAOSPEC/GALA	24
3.6	Chemical abundances from spectral synthesis	25
3.7	Uncertainties	28
3.8	NLTE corrections	29
4	Results	30
4.1	Iron	30
4.2	Carbon and Nitrogen	31
4.3	Sodium	31
4.4	α -elements	33
4.5	Iron-peak elements	36
4.6	r -process elements	39
4.7	s -process elements	41
5	Comparison with previous works	48
5.1	Reggiani et al. (2021)	48
5.2	Mucciarelli et al. (2023a)	50

Chapter 1

Introduction

1.1 The metal-poor stars

Stars are the main actors in producing and recycling metals through subsequent stellar generations within galaxies. This is the reason why the overall metallicity increases with cosmic evolution (Tinsley 1980). The Big Bang nucleosynthesis essentially produced hydrogen, helium and traces of lithium. Therefore, when the first stars formed, they were characterised by zero metal content: these are the so called Population III stars, and they have never been observed so far. In fact, the most metal-poor stars observed so far, despite a very low Fe content, exhibit large amounts of C, indicating these stars formed from a gas already enriched by previous stellar generations (Frebel & Norris 2015). From the ashes of these first stars, some extremely metal-poor stars were formed: they are the oldest stars we have been able to observe, and their observation in the Local Universe consequently provides a unique opportunity to explore the physical conditions of primordial star (SF) formation through the analysis of their chemical properties.

The search for metal-poor stars began few decades ago in the Milky Way (MW), and led to the discovery of some extremely metal-poor stars, i.e. stars with $[\text{Fe}/\text{H}] < -3.0$, down to $[\text{Fe}/\text{H}] \sim -7.0$ in the Galactic halo (Frebel & Norris 2015). Thanks to the advent of the 8-10 meter class telescopes like the Very Large Telescope and the Keck Telescopes, stars of MW satellites became resolvable also with high resolution spectroscopy and reasonable integration times, and this extended the search for metal-poor stars to other galaxies in the Local Group (see Tolstoy, Hill & Tosi 2009 for a review about the properties of dwarf galaxies in the Local Group). Metal-poor stars observations in galaxies different from the MW eventually made possible to understand the chemical enrichment history in galaxies with different SF rate (SFR) or initial mass function, i.e. dwarf and irregular galaxies. Stars with $[\text{Fe}/\text{H}]$ between -3.5 and -2.5 dex have been discovered in irregular, dwarf and ultra-faint dwarf galaxies (Tafelmeyer et al. 2010, Frebel et al. 2016, Simon et al. 2019), expanding our comprehension of the early

chemical enrichment of the Universe and opening a new field of study in astrophysics, nowadays commonly referred to as galactic archaeology.

1.2 The Magellanic Clouds

Within this framework, the Large and Small Magellanic Clouds (hereafter indicated as MCs or the Clouds, or LMC and SMC, respectively) provide a unique and greatly interesting case of study. These two galaxies (with stellar masses of $\sim 2.7 \cdot 10^9 M_\odot$ and $\sim 3.1 \cdot 10^8 M_\odot$ for the LMC and SMC respectively, much larger than any other MW satellite galaxy) are in fact among the closest MW satellites, and they are likely at the first peri-Galactic passage with the MW (Besla et al. 2007, 2010; Kallivayalil et al. 2013; Besla 2015). There are several signatures of their mutual interaction and of the interaction between the Clouds and the MW, such as the Magellanic Bridge, which connects the SMC and the LMC, and the Magellanic Stream, which embraces these two galaxies. The history of the stellar populations of the SMC is intimately linked to the interplay of these three galaxies (Harris & Zaritsky 2004, Bekki & Chiba 2005, Massana et al. 2022): the multiple episodes of SF in their history are likely the result of the periodic close encounters between them.

The stellar content of the MCs is dominated by stellar populations with ages not older than 5-6 Gyr, which aroused from dynamical interactions between the LMC and the SMC. Pagel & Tautvaisiane (1998) computed theoretical age-metallicity relation (AMR) for both the LMC and the SMC, assuming the Clouds have been built up by gradual infall of unprocessed material. The SF history (SFH) of the MCs associated to these models is characterised by an initial burst of SF, ending ~ 12 Gyr ago, with the two galaxies evolving as isolated systems, followed by a quiescent phase of very low SF activity, concluded $\sim 3-4$ Gyr ago by a new, more prominent, common SF burst, most likely caused by the dynamical interaction between the LMC and the SMC. The resulting MCs AMR models reflect the characteristics of their SFHs: SMC stars with ages between ~ 3 and ~ 11 Gyr are then expected to be within a narrow metallicity interval $-1.3 \lesssim [\text{Fe}/\text{H}] \lesssim -1.1$, with slowly increasing metallicity for younger ages. Conversely, younger stars, formed in the second burst of SF, should show a faster increase of $[\text{Fe}/\text{H}]$, even though always subsolar, with decreasing age, while $\sim 12-13$ Gyr old field stars are believed to be characterised by $[\text{Fe}/\text{H}] < -1.7$. The presence of these bursts of star formation has been confirmed by several photometric studies dedicated to reconstruct the star formation history of the MCs (see e.g. Harris & Zaritsky 2004; Noel et al. 2007; Cignoni et al. 2012, 2013, Rubele et al. 2018).

Recently, Massana et al. (2022) showed the presence of multiple SF bursts from the analysis of the LMC and SMC SFHs, computed through the use of SMASH survey deep photometry data. In the SMC, they identified five peaks of SF in the last 3.5 Gyr, happening at ~ 3 , ~ 2 , ~ 1.1 , ~ 0.45 Gyr ago, and currently ongoing. Those peaks of

SF are synchronous to the ones retrieved by Ruiz-Lara et al. (2020) in their study of the SFH of the LMC, and their separation may be indicative of an orbital period of 1 Gyr between the MCs, which has possibly shortened to 0.5 Gyr in the two most recent passages due to dynamical friction. The most prominent of these SF peaks appears to be the one at ~ 2 Gyr, which is more global and centrally concentrated in the case of the SMC, being it the least massive system of the interacting Clouds. All these information of the SFHs of the MCs is visualized in Figure 1.1.

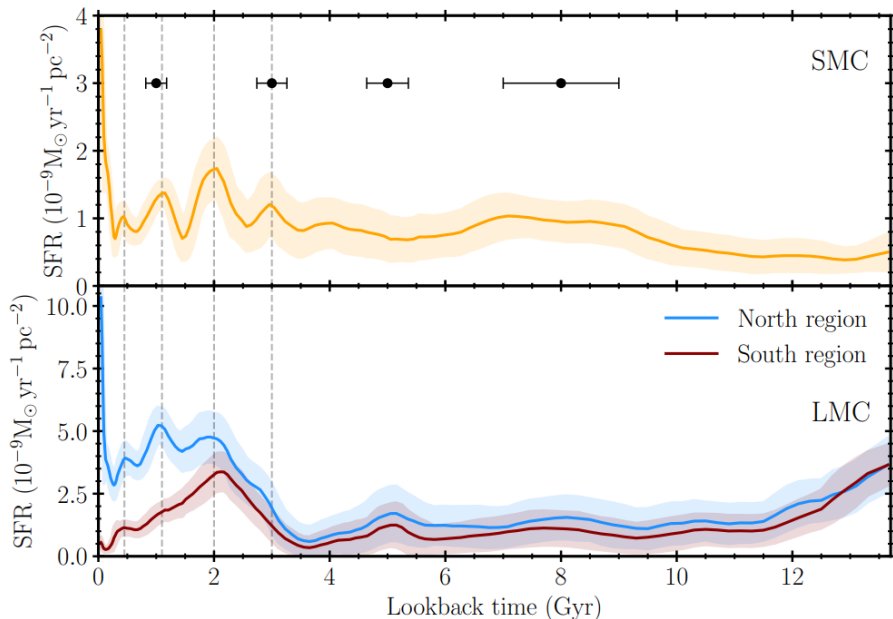


Figure 1.1: Comparison of the global SFRs for the SMC (Massana et al. 2022) and the LMC (Ruiz-Lara et al. 2020). Vertical dashed lines link the peaks at 0.45, 1.1, 2 and 3 Gyr ago in the SMC to those of the LMC. The horizontal bars in the top panel show the width of the SFH enhancement. (Massana et al. 2022).

Despite their unicity among Local galaxies and their proximity (allowing us detailed resolved photometric and spectroscopic observations), our knowledge of the chemical characterization of the MCs stellar populations is restricted to the dominant ones, i.e. intermediate-age and metal-rich stars (Mucciarelli et al. 2008, Pompeia et al. 2008, Lapenna et al. 2012, Van der Swaelmen et al. 2013, Nidever et al. 2020).

1.3 Metal-poor stars in the Magellanic Clouds

Information about the oldest stellar populations and early chemical evolution of the LMC is provided by observations of its old GCs. The LMC, in fact, harbors a population of

15 GCs with ages comparable with those of the MW ones (12-13 Gyr, Brocato et al. 1996; Olsen et al. 1998; Wagner-Kaiser et al. 2017) and ranging from $[\text{Fe}/\text{H}] \sim -2.1$ and -1.2 (Mucciarelli et al. 2021b). Johnson et al. (2006) observed ten red giant branch (RGB) stars in four old LMC GCs (NGC 1898, NGC 2005, NGC 2019, Hodge 11) with the high-resolution spectrograph MIKE at the Magellan Telescope. From the analysis of these high-resolution spectra, they confirmed the metal-poor $[\text{Fe}/\text{H}]$ abundance of these old clusters (the most metal-poor one being Hodge 11 with $[\text{Fe}/\text{H}] \sim -2.1$), as well as they determined abundances for up to 20 between α , light odd- Z , iron-peak and neutron-capture elements. The authors found some abundance similarities between LMC GCs and MW clusters, but also some marked differences in the abundances of some α and some iron-peak elements, which were interpreted as emerging from a unique chemical enrichment history, different from those of the MW and of dwarf spheroidal galaxies in the Local Group.

Mucciarelli et al. (2010) presented the chemical abundance analysis of UVES-FLAMES and GIRAFFE-FLAMES spectra of eighteen giant stars belonging to three other old GCs in the LMC (NGC 1786, NGC 2210, NGC 2257). They confirmed the metal-poor nature of those clusters, with NGC 2257 being the most metal-poor of the three ($[\text{Fe}/\text{H}] = -1.95$), and found abundance ratios in agreement with Galactic GCs for α and iron-peak elements at similar $[\text{Fe}/\text{H}]$. Conversely, all the three clusters showed a relevant depletion of $[\text{Y}/\text{Fe}]$ and a $[\text{Eu}/\text{Fe}]$ enhancement with respect to Galactic distributions. These ratios were interpreted as the result of a very efficient r -process element production, while the less prominent s -process element production caused by the missing AGB stars chemical enrichment at early times, i.e. in these very old clusters, is favouring the formation of heavy s -process elements, like Ba, over light s -process element, like Y.

The study of the oldest LMC GCs, taking advantage of the substantially coeval and chemically homogeneous nature of these systems within each of these stellar populations, eventually shed some light on the early chemical enrichment of the LMC, highlighting some similarities and differences with the MW, Galactic clusters and dwarf spheroidal galaxies. The same approach cannot unfortunately be applied in the search for metal-poor stars of the SMC. At variance with LMC and MW, there are no GCs in the SMC old like those observed in the LMC and MW. Glatt et al. (2008) provide absolute and relative age determination of the oldest SMC GC, NGC 121, whose location with respect to the SMC can be seen in Fig.1.2. Exploiting Hubble Space telescope observation of NGC 121 with the ACS instrument in the F555W and F814W filters, they produced a CMD reaching ~ 3.5 mag below its main sequence turn-off. They fitted various isochrones to NGC 121 observed ridge line and measured absolute ages between 10.5 ± 0.5 Gyr and 11.8 ± 0.5 Gyr. Their relative age measurements from the magnitude difference between the main-sequence turn-off and the horizontal branch, and from the absolute magnitude of the horizontal branch, provide ages of 10.9 ± 0.5 Gyr and 11.5 ± 0.5 Gyr, respectively, and are consistent with the absolute age measurements. The age estimates from the ACS photometric data of NGC 121 show this cluster is consistently 2-3 Gyr younger than the

oldest Galactic GCs, whose absolute age is ~ 13 Gyr (Krauss & Chaboyer 2003), and LMC GCs. A chemical analysis of NGC 121 is provided by Mucciarelli et al. (2023b): they measure $[\text{Fe}/\text{H}] = -1.18 \pm 0.02$ and almost solar $[\alpha/\text{Fe}]$ abundances, indicating that this cluster formed from gas already enriched by SNe Ia, in agreement with its age estimates and not providing information on the first stellar generations.

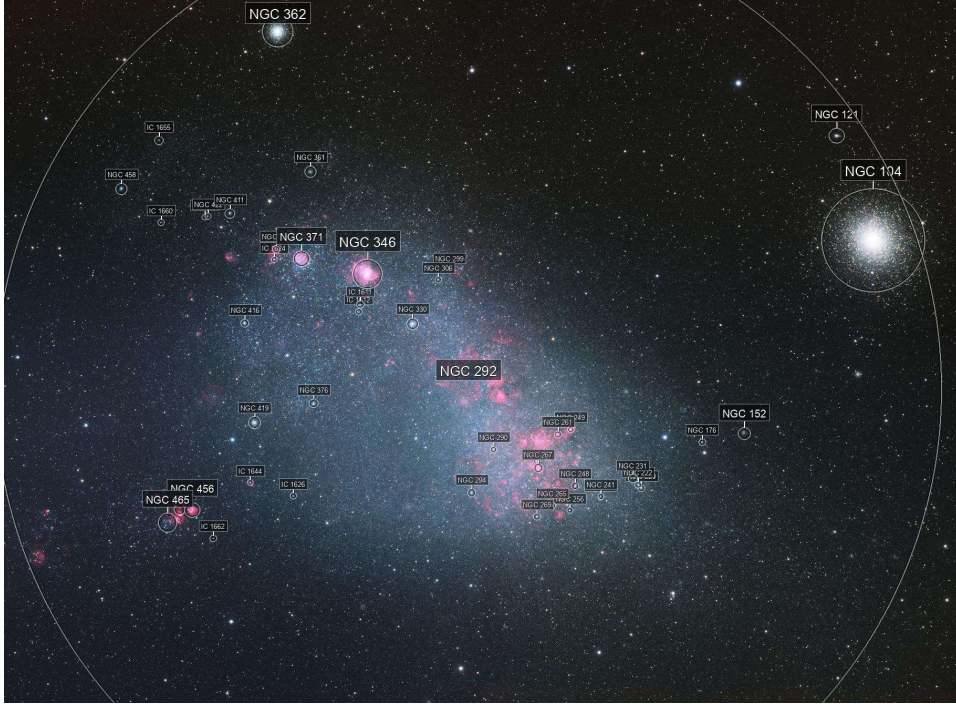


Figure 1.2: Optical image of the SMC with marked positions of the most massive GCs. It is possible to see the oldest SMC GC, NGC 121, in the top right part of the image, slightly above NGC 104/47 Tucanae

The lack of old GCs in the SMC requires to look for some sufficiently metal-poor stars among its field stars in order to obtain some information on its first chemical enrichment, happening ~ 13 Gyr ago. However, the AMRs computed for the MCs, together with a sufficiently large number of observed member stars, made clear how the younger stellar population emerging from the dynamical interactions between the LMC and the SMC accounts for almost the whole present stellar content of the MCs themselves: this fact further complicates the identification of metal-poor field stars and the study of their early chemical enrichment. Nidever et al. (2020) presented metallicities and α -element abundances for 3600 RGB stars across the entire extensions of the two galaxies using near-infrared medium resolution ($R \sim 22,500$) APOGEE spectra. Despite the large sample of RGB stars and an advancement in the characterisation of the $[\alpha/\text{Fe}]$ - $[\text{Fe}/\text{H}]$ distribution (Figure 1.3), they were only able to indicate an upper limit to constrain the α -knee

position, in both the LMC and the SMC, to $[\text{Fe}/\text{H}] \sim -2.2$. However, these data were not offering clear evidence of a high- α plateau, also because of the small number of stars with $[\text{Fe}/\text{H}] < -1.7$ (see the $[\text{Fe}/\text{H}]$ distribution in Figure 1.4) in both Clouds, even though the sample was an order of magnitude larger than in previous studies and extended to larger radial distances.

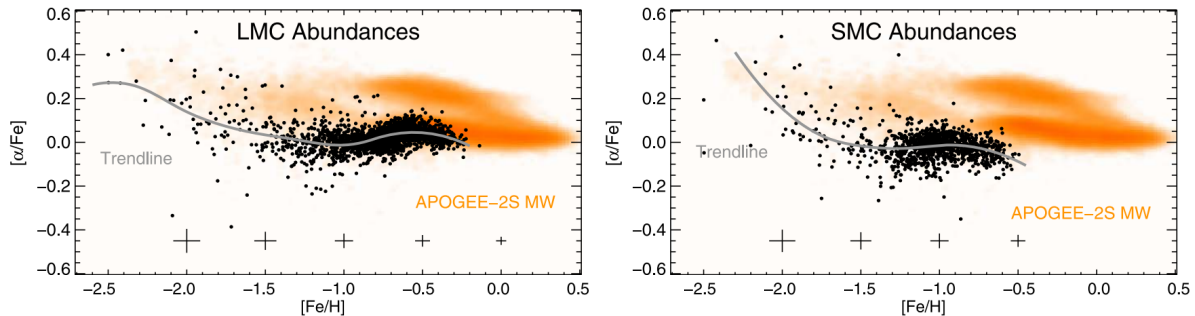


Figure 1.3: The α abundances of the MCs ($[\alpha/\text{Fe}]$ vs. $[\text{Fe}/\text{H}]$). (Left) LMC and (right) SMC with the APOGEE MC shown as black filled circles. Density of APOGEE-2S MW stars (orange) and a B-spline trend line for the MC stars (gray). (Nidever et al. 2020).

A procedure of selection of metal-poor stars based on a different kind of photometric selection was performed in Reggiani et al. (2021). Here, the authors selected an initial list of candidate metal-poor giants belonging either to the LMC or the SMC, using a variant of the Schlafman & Casey (2014) infrared metal-poor star selection on Two Micron All Sky Survey (2MASS) near-infrared and Spitzer SAGE or AllWISE mid-infrared photometry. They subsequently found literature data for four of their LMC metal-poor candidate stars and confirmed the metal-poor nature of four of their SMC candidates using FLAMES-GIRAFFE data from Mucciarelli (2014). They supplemented their sample with three additional LMC candidate metal-poor stars, based on low Ca II-inferred metallicities from Carrera et al. (2008), and eventually implemented two LMC stars from SDSS APOGEE-2 with inferred metallicities in the range $-1.7 \lesssim [\text{Fe}/\text{H}] \lesssim -1.5$. This sample of nine LMC and four SMC candidate metal-poor stars was addressed a high-resolution spectroscopic follow-up with the Magellan MIKE spectrograph. They found the four SMC giants to have metallicities in the range $-2.6 \lesssim [\text{Fe}/\text{H}] \lesssim -2.0$, making them the most metal-poor stars in the MCs yet subject to a comprehensive abundance analysis. Although these metal-poor stars look similar to MW stars of similar $[\text{Fe}/\text{H}]$ in their α , light and iron-peak elemental abundances, they exhibit an enhancement in the r -process element europium. The authors remark how this offset in europium abundance of SMC stars with respect to MW stars is highly significant (2.7σ) and it is even more remarkable for LMC stars (3.9σ) and for the whole MCs sample of spectra (5.0σ). This greater abundance of europium at lower metallicities was interpreted as

the result of the MCs isolated chemical evolution and long history of accretion from the cosmic web, combined with r -process nucleosynthesis on a timescale longer than the type II supernova timescale but shorter or comparable to the type Ia supernova timescale.

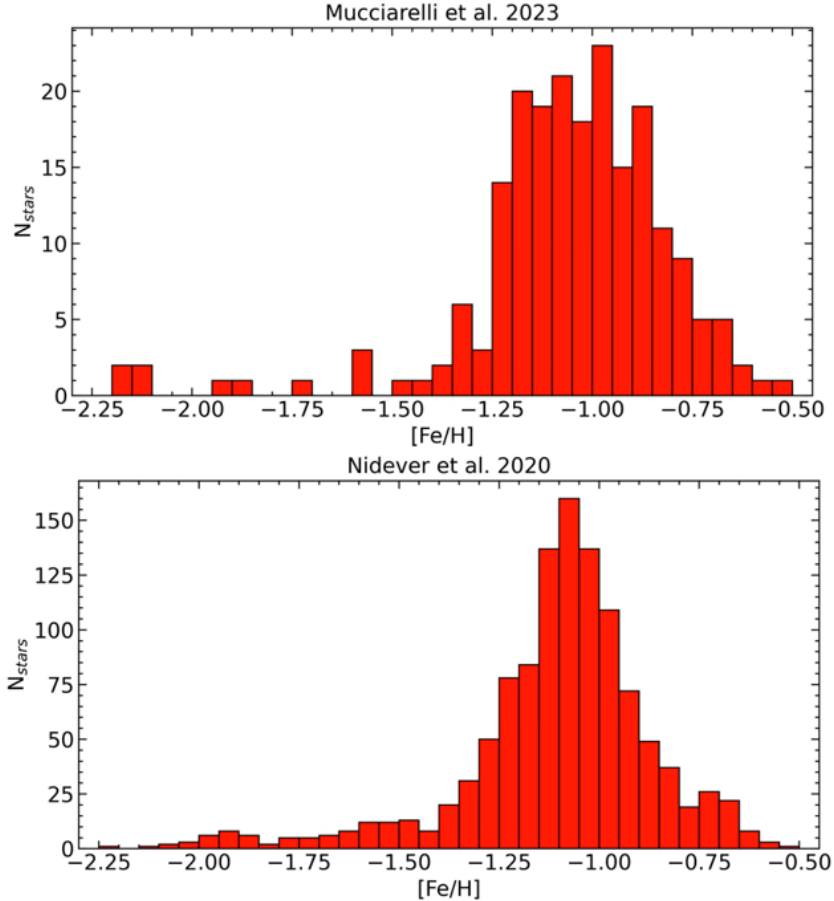


Figure 1.4: $[\text{Fe}/\text{H}]$ distributions of 206 RGB SMC stars from Mucciarelli et al. (2023a) and of 1143 RGB SMC stars from Nidever et al. (2020).

Mucciarelli et al. (2023a) presented the chemical composition of 206 RGB SMC member stars from three different regions around three SMC GCs (NGC 121, NGC 339, NGC 419), obtained using optical spectra taken with FLAMES-GIRAFFE at the Very Large Telescope. The metallicity distribution from this sample confirms how difficult is to find metal-poor targets, since the stellar content is dominated by metal-rich (likely intermediate-age) stars of the SMC, in all the three observed fields, similarly to distributions obtained from low-resolution spectra with the use of CaII triplet as a metallicity indicator (Carrera et al. 2008, Dobbie et al. 2014a, b, Parisi et al. 2016) and in Nidever et al. (2020). The entire sample peaks at $[\text{Fe}/\text{H}] \sim -1.0$ and 95% of the observed stars have metallicities in the range $-1.5 < [\text{Fe}/\text{H}] < -0.5$, with a weak metal-poor tail ex-

tending down to $[\text{Fe}/\text{H}] \sim -2.2$ (Figure 1.4). However, $\sim 20\%$ of the stars of the sample in the region surrounding NGC 121 exhibit $[\text{Fe}/\text{H}] < -1.5$, while only one star per field satisfies the same criterion in the regions around NGC 339 and NGC 419.

Chiti et al. (2024) performed a search and analysis of low-metallicity stars in the LMC by applying metallicity sensitive photometric selections to data from Data Release 3 of the Gaia mission. They identified LMC metal-poor candidate stars using a metallicity-sensitive color-color relation developed in Chiti et al. (2020) from Gaia photometric filters, including the filter centered on the CaHK feature. The Ca H and K strong absorption features can in fact cause a sensible decrease of the measured flux in the related photometric filter and can be exploited to get a first estimate of the calcium content of a star, which is in turn a first rough indicator of the metallicity and of the $[\text{Fe}/\text{H}]$ content of the observed target. The authors identified ten metal-poor candidate stars suitable for high-resolution follow-up and observed them with the Magellan MIKE spectrograph, getting abundances in the range $-4.2 < [\text{Fe}/\text{H}] < -2.5$ and unveiling unprecedented information on the early chemical enrichment of the LMC. The LMC appears to have had an inefficient star formation or gas inflows, with a α -element trend clearly discrepant from the MW: the α -knee location was constrained at $[\text{Fe}/\text{H}] < -1.82$, significantly lower than what is expected ($[\text{Fe}/\text{H}] \sim -1.2$) for a galaxy as massive as the LMC. A similar spectroscopic approach can possibly be applied to the SMC as well, knowing it also shares a common chemodynamical evolution pattern with the LMC.

1.4 The aim of this work

As previously discussed, studies based on high-resolution spectra of metal-poor stars have been published in the last few years. Unfortunately, our current knowledge of the chemical enrichment of the early stages of these galaxies is still limited, particularly for the SMC, due to the lack of GCs with ages of 12-13 Gyr. According to the Pagel & Tautvaisiane (1998) theoretical AMR, the oldest stars in the SMC should have $[\text{Fe}/\text{H}]$ below $-1.7/ -1.8$ (see Figure 1.5).

The APOGEE survey from Nidever et al. (2020) has identified a few dozen stars with $[\text{Fe}/\text{H}]$ between -2.3 and -1.7 dex, but the infrared spectral region is not suitable for providing precise abundances for such metal-poor stars due to the weakness of the lines in this spectral range. The metal-poor stars observed in optical bands (Mucciarelli et al. 2023a and Reggiani et al. 2021) are still based on a resolution of about 20,000 and often have a low signal-to-noise ratio (SNR), as it can be appreciated in Figure 1.6.

This study arises from the need to measure chemical abundances in SMC metal-poor stars (thus among its oldest stars) by simultaneously combining high spectral resolution, high SNR, and wide spectral coverage, in order to adequately sample a large number of chemical elements. From their medium resolution analysis, Mucciarelli et al. (2023a) identified a sample of seven metal-poor stars that have been then observed with the spec-

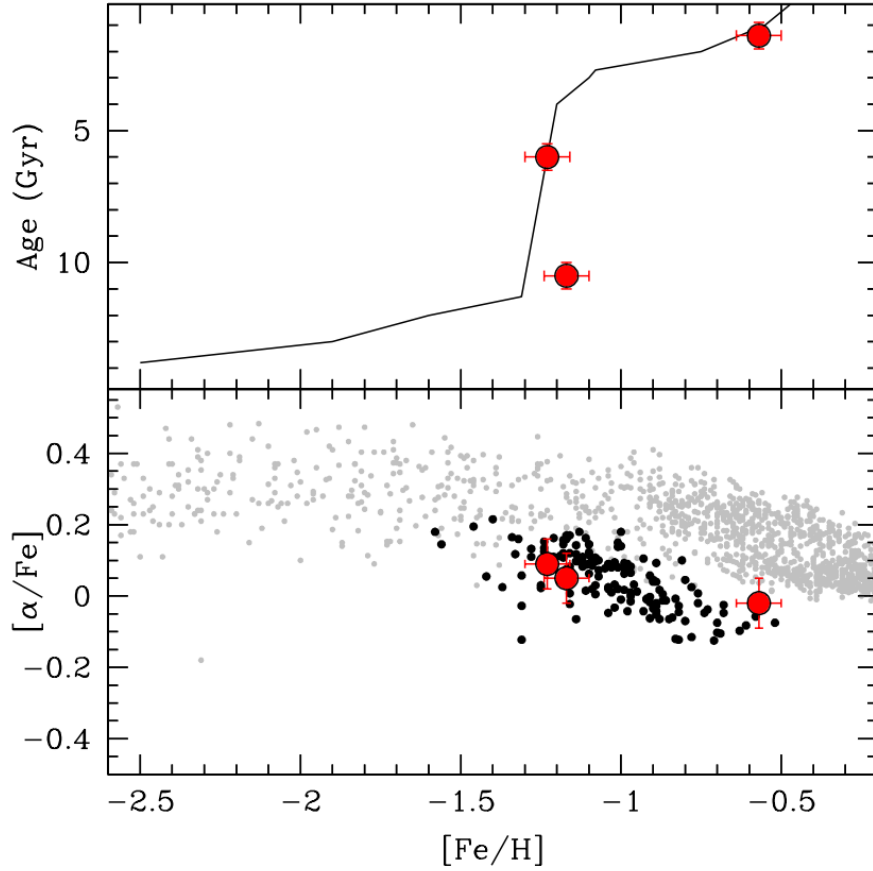


Figure 1.5: Upper panel: age-metallicity relation for the SMC GCs (red circles) in comparison with a theoretical model. Lower panel: $[\alpha/\text{Fe}]$ as a function of $[\text{Fe}/\text{H}]$ for the SMC field stars (black points), SMC GCs (red circles) and MW stars (grey points). Chemical abundances are from Mucciarelli et al. (2023a, b).

trograph UVES@VLT, providing spectra with high resolution ($R \sim 40,000$) and $\text{SNR} \sim 60$, together with a large spectral coverage, in order to provide a detailed chemical analysis of metal-poor SMC stars. The main aims of this chemical analysis are:

- to characterize the contribution at the early chemical enrichment of the SMC of the main chemical contributors, in particular massive stars exploding as core collapse SNe (CC-SNe), thermonuclear SNe (SNe Ia), AGB stars, neutron star mergers;
- to estimate the level of homogeneity of the chemical abundances at low metallicities, as indicator of the mixing of the gas;
- to compare the chemical composition of the old, metal-poor SMC stars with MW stars of similar metallicity, in order to highlight differences and similarities of their

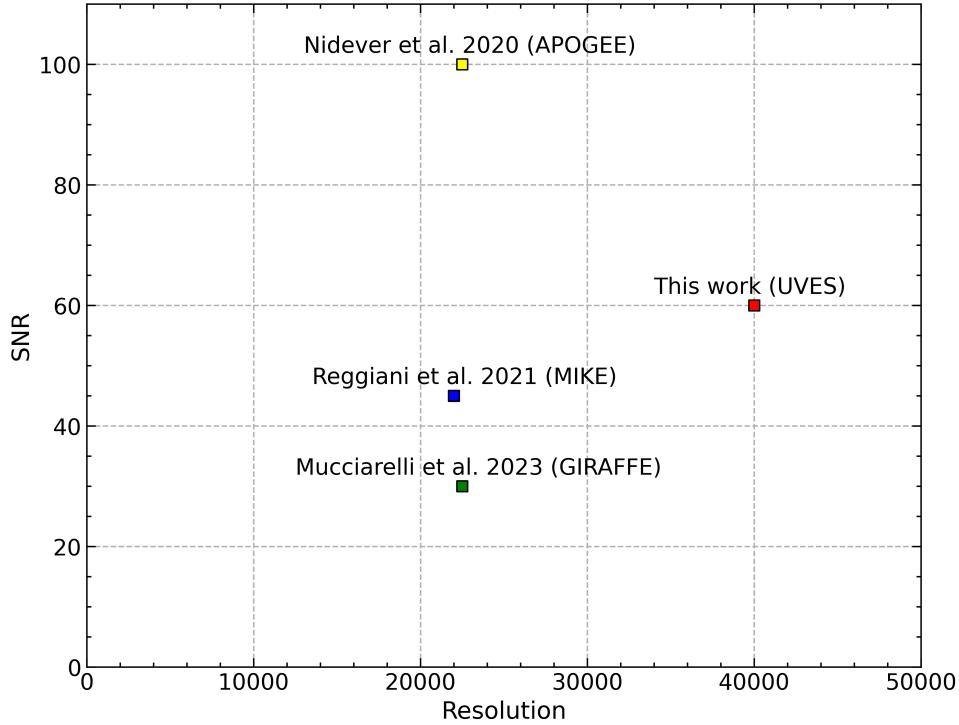


Figure 1.6: Spectral resolution and SNR of the spectroscopic samples of metal-poor SMC stars discussed in the literature (Nidever et al. 2020, Reggiani et al. 2021, Mucciarelli et al. 2023a) and of this study.

chemical enrichment histories.

The work is organised in the following way: initially, a description of the used spectroscopic dataset is provided; then, the analysis of the adopted atmospheric parameters and synthetic spectra, measured radial velocities, implemented line selection and methods used for the abundances computation is thoroughly explained; subsequently, results of the chemical analysis are discussed and compared with other studies done on the same targets; finally, some conclusions about the early chemical enrichment of the SMC emerging from this chemical analysis are advanced.

Chapter 2

Spectroscopic Dataset

This work presents the analysis of a spectroscopic dataset including seven metal-poor RGB stars identified by Mucciarelli et al. (2023a) through the analysis of medium resolution FLAMES-GIRAFFE spectra. According to Mucciarelli et al. (2023a), these stars have abundances in the interval $-2.2 < [\text{Fe}/\text{H}] < -1.7$, compatible with the first chemical enrichment of the SMC, happening $\sim 12 - 13$ Gyr ago, as suggested by the theoretical AMR for the SMC presented by Pagel & Tautvaisiane (1998). However, the chemical analysis of these metal-poor stars would certainly benefit from a high-resolution spectroscopic follow-up: the resolution of FLAMES-GIRAFFE spectra is about 20,000 and the available spectra have a limited spectral coverage (~ 600 Å in total, considering two different spectral regions), allowing to measure a limited number of elements.

The seven metal-poor stars were observed with the spectrograph UVES (Dekker et al. 2000) mounted at the Very Large Telescope of ESO. The observations were carried out between May and August 2023 under the program 111.24Z9 (PI: Mucciarelli), using the UVES Red Arm CD3 580 setting and the 1" slit, providing high-resolution ($R=40,000$) and wide coverage ($4760\text{Å} < \lambda < 6840\text{Å}$) spectra, together with a $\text{SNR} \sim 60$. The adopted setting is composed by the chips observing simultaneously and providing two spectra of about 1000Å of coverage each and separated by a small wavelength gap. We refer to these two spectra as REDL (Red Arm lower chip, $4760\text{-}5760\text{Å}$) and REDU (Red Arm upper chip, $5800\text{-}6840\text{Å}$). Moreover, the use of UVES in the Dichroic1 mode allowed to simultaneously observe the stars using the Blue Arm CD2 390 setting and extended the spectral coverage to bluer wavelengths ($3260\text{Å} < \lambda < 4540\text{Å}$), enabling to observe some molecular bands absorption features, such as those from CH and CN, and get some information on the carbon and nitrogen content of this sample.

For each target several exposures of 50 min each (between 3 and 5 according to the target magnitude) were secured. The SNR of the combined spectra is ~ 50 per pixel at 5300Å and ~ 60 per pixel at 6300Å . The use of a slit spectrograph allows to simultaneously extract the sky background spectrum together with the source spectrum. Therefore, the sky background is subtracted from the extracted spectrum for each indi-

vidual exposure. Then, sky-subtracted spectra of the same star are combined together in order to increase the SNR. All the individual spectra were corrected for the heliocentric correction, so that the shift showing up in the absorption features of each star spectrum is only due to their radial velocity, and no effect due to the motion of Earth around the Sun is left. Figure 2.1 shows, as an example, a set of combined spectra, after background subtraction and heliocentric correction, for one of the targets; one spectrum is obtained from the Blue Arm adopted setting and other two spectra are obtained from the two halves of the Red Arm adopted setting.

The list of the targets with their coordinates, GAIA DR3 identification number and G magnitudes and the number of single exposures they were dedicated is shown in Table 2.1. Six of the seven targets were observed in an outer SMC region, in the field around the old GC NGC 121, while one target is located in a central region of the galaxy, more precisely in the field near the cluster NGC 419. The spatial distribution of the observed metal-poor candidate stars in the SMC can be visualized in Figure 2.2. We reported in Figure 2.3 the position of the targets in the GAIA DR3 color-magnitude diagram of the field they respectively belong to. Four of these seven metal-poor SMC stars were already targeted for Magellan MIKE high resolution spectroscopy in Reggiani et al. (2021): they are FLD-121_100330, FLD-121_100514, FLD-121_100683, FLD-121_100781. The MIKE spectra of these four stars are characterised by a spectral resolution $R \sim 22,000$ and an average SNR ~ 45 at 6500\AA .

Target	GAIA DR3 ID	RA (deg)	Dec (deg)	G (mag)	N_{exp}
FLD-121_100330	4689859031717528576	6.5997764	-71.4819327	16.82	5
FLD-121_100514	4689864941592504064	6.6650025	-71.3695227	16.14	3
FLD-121_100683	4689861093301638272	6.9064647	-71.4198831	16.00	3
FLD-121_100767	4689844153950876928	6.5164312	-71.6726397	16.44	4
FLD-121_100781	4689844875502755328	6.3269777	-71.6687564	15.94	3
FLD-121_100823	4690236267283684992	7.1733613	-71.3943678	16.55	5
FLD-419_1355	4687224842392729984	17.0954359	-72.8907066	16.54	4

Table 2.1: List of targets observed with the UVES spectrograph, together with their GAIA DR3 identification numbers, RA and Dec coordinates, G magnitudes and number of exposures.

Additionally, we analysed one MW star of metallicity and stellar parameters similar to those of our SMC targets. This star, namely BD06448, has been selected from the SAGA database (Suda et al. 2008) searching for giant stars in the bright part of the RGB and in the $[\text{Fe}/\text{H}]$ between -2.3 and -1.7 . We selected this star because spectra obtained with UVES in the same spectral configuration of the SMC targets are available in the ESO archive.

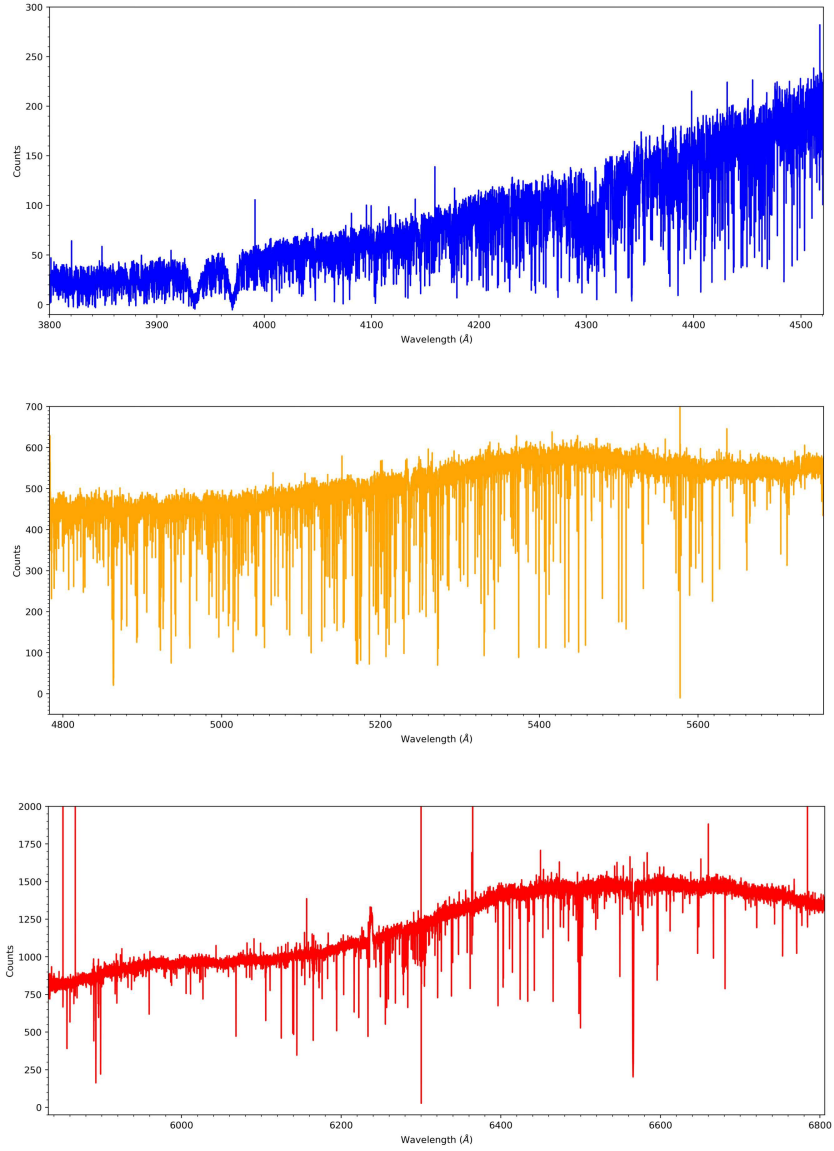


Figure 2.1: UVES combined spectra for the target FLD-121_100330, after background subtraction and heliocentric correction. The upper spectrum was obtained from the Blue Arm setting exposures, the central and lower spectrum were obtained from the Red Arm setting exposures.

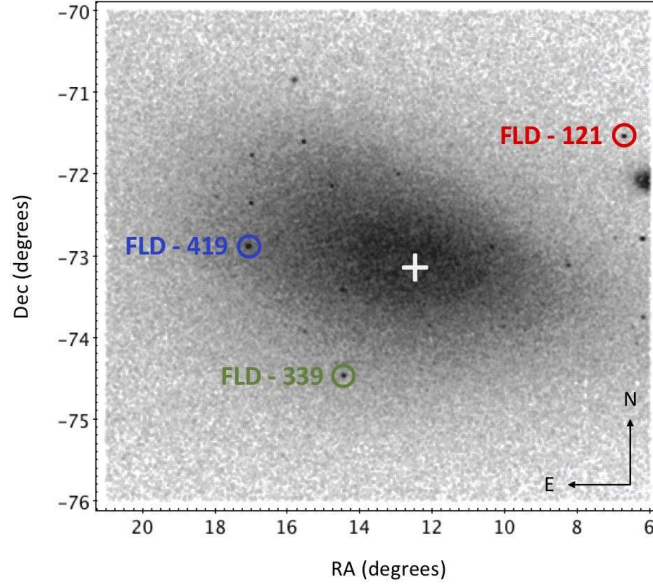


Figure 2.2: Spatial distribution of the three fields observed with FLAMES by Mucciarelli et al. (2023a) (red, green, and blue circles for FLD-121, FLD-339, and FLD-419, respectively), superimposed on the map of the SMC RGB stars with G magnitude between 16 and 19 from Gaia EDR3 (Gaia Collaboration 2021), revealing the old spheroid of the SMC. The white plus marks the position of the SMC centre derived by Ripepi et al. (2017).

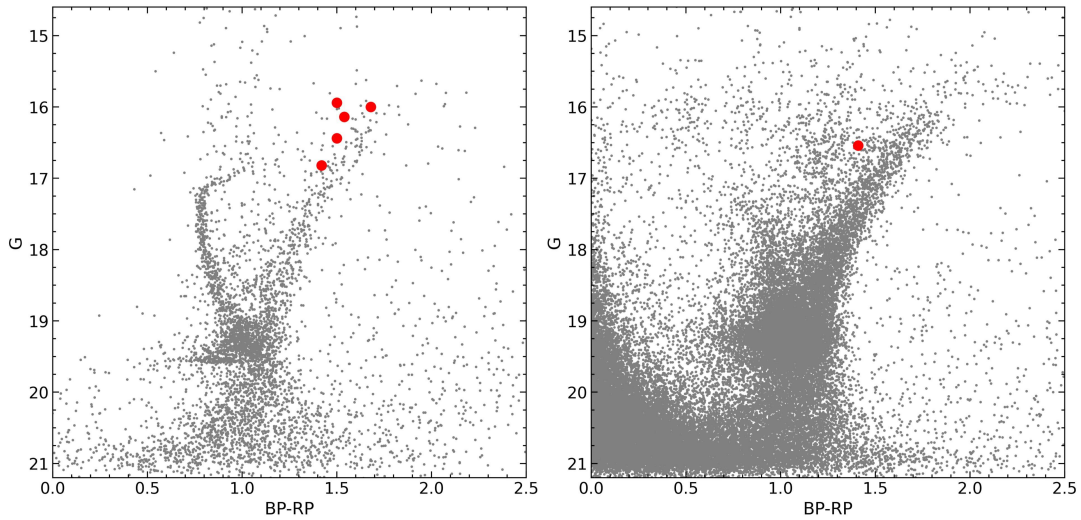


Figure 2.3: Color Magnitude Diagrams of SMC fields around NGC 121 (left) and NGC 419 (right); field 121 targets are reported in red, field 419 target is reported in green.

Chapter 3

Spectroscopic Analysis

The analysis of the available spectroscopic dataset includes: the estimate of the atmospheric parameters of the observed targets; the measure of their radial velocities; the line selection procedure; the actual computation of chemical abundances.

3.1 Atmospheric parameters

We adopted the same values computed by Mucciarelli et al. (2023a) for T_{eff} and $\log g$ since they are based on data from GAIA DR3 photometry (Gaia Collaboration 2021), which offer the most precise photometry, and therefore the best temperatures and surface gravities estimates, at present time. For the seven stars of our sample, we made use of the atmospheric parameters computed in Mucciarelli et al. (2023a), reported in Table 3.1. In their work, T_{eff} were obtained from the broad-band color $(G - K_s)_0$, adopting the transformation described and reported in Mucciarelli et al. (2021a), exploiting GAIA EDR3 G magnitudes (Gaia Collaboration 2018), 2MASS K_s magnitudes (Skrutskie et al. 2006) and colour excess values $E(B - V)$ from infrared dust maps (Schlafly & Finkbeiner 2011). The effective temperatures are characterised by uncertainties of $\sim 50 - 60$ K, including the uncertainty of the calibration itself (the dominant source of error), the error in the $G - K$ color and that in the color excess. The $\log g$ values were computed through the Stefan-Boltzmann relation, using the previously computed T_{eff} , a true distance modulus $(m - M)_0 = 18.965 \pm 0.025$ (Graczyk et al. 2014), bolometric corrections computed according to Andrae et al. (2018), and stellar masses of $1.0 \pm 0.2 M_\odot$. The $\log g$ errors are dominated by the stellar masses ones and are of the order of 0.1. For the computation of the microturbulence velocity values v_t , they were computed using $\log g - v_t$ relations from Mucciarelli & Bonifacio (2020), in order to avoid large v_t fluctuations in their spectroscopical determination, potentially caused by the small number of available Fe I lines or bias against the weak lines because of the SNR of the spectra. The error associated to v_t is about 0.2 km s^{-1} , considering the uncertainty of

the relation and the error in $\log g$. The stellar parameters of the MW comparison star have been derived with the same approach, using Gaia photometry and the color- T_{eff} transformation by Mucciarelli et al. (2023a), adopting the color excess from the dust extinction maps by Lallement et al. (2022) and adopting the distance from the Gaia parallax.

Target	T_{eff} (K)	$\log g$ (cgs)	v_t (km s⁻¹)
FLD-121_100330	4424	1.09	1.7
FLD-121_100514	4274	0.73	2.2
FLD-121_100683	4201	0.63	2.3
FLD-121_100767	4298	0.86	1.8
FLD-121_100781	4152	0.57	1.9
FLD-121_100823	4133	0.80	1.8
FLD-419_1355	4300	0.85	1.8
BD06448 (MW)	4492	1.07	1.7

Table 3.1: List of targets observed with the UVES spectrograph, together with their atmospheric parameters T_{eff} , $\log g$ and v_t . The values reported here and used in the subsequent analysis are the ones obtained by Mucciarelli et al. (2023a).

Thanks to the larger number of iron lines provided by the UVES spectra with respect to GIRAFFE spectra in Mucciarelli et al. (2023a), we attempted at spectroscopically derive the stellar parameters by: erasing the trends between abundances resulting from the absorption lines and their excitation potential, which can be caused by wrong T_{eff} ; erasing the trends between abundances and absorption lines reduced equivalent widths, which can indeed be caused by wrong v_t values (especially for saturated lines); removing the difference in abundances from Fe I and Fe II lines, mainly by adjusting the $\log g$ value.

The T_{eff} and $\log g$ we obtained with this spectroscopic approach are systematically lower than the values from Gaia photometry, by 250-300 K for T_{eff} and by more than 0.5 for $\log g$. For metal-poor stars, the spectroscopic computation of atmospheric parameters usually leads to values of T_{eff} and $\log g$ characterised by progressively larger differences with respect to the same parameters computed with a photometric approach. At $[\text{Fe}/\text{H}] = -2$, a metallicity comparable with the stars analysed in this work, spectroscopic T_{eff} and $\log g$ can respectively be 300 K and 0.5 lower than the photometric values, as shown by Frebel et al. (2013) and Mucciarelli & Bonifacio (2020). This constitutes a significant difference with respect to photometrically determined T_{eff} and $\log g$ values, which are more accurately describing the actual physical conditions of the observed targets stellar atmospheres, also due to the high quality of GAIA photometry.

We therefore attempted at spectroscopically deriving only the v_t parameter, after fixing T_{eff} and $\log g$ at their photometrically computed values. On the contrary of T_{eff}

and $\log g$ measurements, this was done because, given the sample of more than 100 unblended Fe I lines over a 2000\AA spectral range for each star, we expect to get reliable estimates of the microturbulence parameter, even if doing so on metal-poor targets. By leaving v_t as a free parameter, we obtained microturbulence values which are consistent with those computed using $\log g - v_t$ relations from Mucciarelli & Bonifacio (2020): in light of this, we eventually decided to go on with our analysis by sticking with the full set of their atmospheric parameters and errors.

We conclude the description on the atmospheric parameters by comparing the values we adopted from Mucciarelli et al. (2023a) with the ones used by Reggiani et al. (2021) on their analyses of 4 SMC stars in common with our sample. In this study, classical excitation/ionization balance was combined with the use of isochrones, in order to avoid the offset caused by the spectroscopic computation of photospheric stellar parameters, described in Mucciarelli & Bonifacio (2020) and known to be relevant in the determination of metal-poor star temperatures and gravities.

Reggiani et al. (2021) first determined a set of atmospheric stellar parameters from the classical excitation/ionization balance analysis, then calculated new T_{eff} and $\log g$ values through the use of isochrones from targets positions on CMDs, and used these two last values to self-consistently determine metallicity $[\text{Fe}/\text{H}]$ and microturbulence v_t from the equivalent widths of the available iron lines from their spectra. This process alternating the use of isochrones and spectroscopic analysis was iterated until metallicities compatible within the uncertainties were found from the two analyses. The average difference between our parameters and those derived by Reggiani et al. (2021) are -130 ± 60 K in T_{eff} , $0.04 \pm 0.06 \text{ cm s}^{-2}$ in $\log g$ and $-1.0 \pm 0.2 \text{ km s}^{-1}$ in v_t . The comparison of the abundances derived in this study and by Reggiani et al. (2021) will be discussed in section 5.1. Here we note as the significant differences in parameters, especially in v_t (at a level of 5σ) is the main responsible of the abundance differences we found with that work.

3.2 Computation of synthetic spectra

The basic tool in the analysis of stellar spectra is the computation of appropriate synthetic spectra, with specific atmospheric parameters and chemical mixture. Given the fundamental role of synthetic spectra in the determination of chemical abundances, we provide a description of the main theoretical tools implemented for their computation. Each synthetic spectrum was computed by means of the code SYNTHE (Sbordone et al. 2004, Kurucz 2005), using ATLAS9 model atmospheres (Castelli & Kurucz 2003). The ATLAS9 code is used for the computation of model atmospheres, adopting one-dimensional, plane-parallel geometry and assuming LTE for all the chemical species. A model atmosphere is defined according to the following parameters: effective temperature (T_{eff}), surface gravity ($\log g$), microturbulent velocity (v_t) and chemical mixture

(metallicity and α -elements abundance).

The code SYNTHÉ calculates a synthetic spectrum based on input stellar parameters associated to an ATLAS9 model atmosphere, linelists of all the included atomic and molecular transitions, and a chemical mixture that can be coincident with that of the model atmosphere or have some differences specified by the user. The synthetic spectrum is then broadened by convolution with a Gaussian profile to reproduce the observed instrumental broadening ($R=40,000$), which is much lower than the native resolution (600,000) at which the synthetic spectra are computed.

3.3 Radial velocities

We measured radial velocities (RV) from the stellar spectra of our sample using the cross correlation (CC) technique (see e.g. Tonry & Davis 1979). We made use of the PyAstronomy package in a Python code that computes a CC function by shifting the observed spectrum of each star over a template spectrum. As a template, we adopted a synthetic spectrum, computed as described above, assuming the typical parameters of our targets ($T_{eff} = 4250$ K, $\log g = 0.8$, $v_t = 1.9$ km s $^{-1}$), a metallicity of $[M/H] = -2.0$ (the average of the $[Fe/H]$ values for the same sample of stars from Mucciarelli et al. (2023a) was employed as a starting metallicity value), solar $[\alpha/Fe]$ mixture. The computation of the CC function was done for RV values in a fairly large interval ($50 < RV < 250$ km s $^{-1}$), shifting the observed spectra by 0.1 km s $^{-1}$ each time. The main peak of the CC function is identified, corresponding to the most probable RV shift for that star. We got two RV values from the CC of two observed spectra halves of the Red Arm CD3 580 UVES setting, one for the REDL and one for the REDU, which we averaged into a single RV value for each star of the sample. The errors associated to those RV values are of 0.05 km s $^{-1}$ and were computed by means of a MonteCarlo simulation.

Target	RV_{CC} (km s $^{-1}$)	RV_{Mu+23} (km s $^{-1}$)
FLD-121_100330	137.10 \pm 0.05	139.3 \pm 0.3
FLD-121_100514	155.95 \pm 0.05	155.2 \pm 0.1
FLD-121_100683	150.95 \pm 0.05	153.3 \pm 0.1
FLD-121_100767	119.20 \pm 0.05	119.8 \pm 0.3
FLD-121_100781	106.00 \pm 0.05	106.0 \pm 0.3
FLD-121_100823	179.00 \pm 0.05	181.6 \pm 0.3
FLD-419_1355	139.50 \pm 0.05	140.3 \pm 0.2

Table 3.2: List of targets observed with the UVES spectrograph, together with average CC RV computed from the REDL and REDU halves of the observed spectra, and RV computed from GIRAFFE spectra by Mucciarelli et al. (2023a).

The values of RV obtained for each star are reported in Table 3.2. We checked that

the wavelength calibration has been carried out correctly on the raw spectra from single exposures of each star, before the application of heliocentric correction and sky subtraction, by looking for the position of some atmospheric emission and absorption lines. In the REDL spectra we used the 5577.3Å O I emission line, while in the REDU spectra we relied on the position of the 6300.3Å O I emission line and a series of atmospheric absorption lines clearly visible in the REDU observed spectra. We performed a CC also on these two features, finding Doppler shifts compatible with zero and ruling out systematics in the zero-points of the wavelength scale.

The obtained values of RV confirm those stars are not members of the GCs near which they were observed, but field stars belonging to the SMC itself. However, some RV from UVES spectra show differences with respect to RV from GIRAFFE data for the same targets. To understand how significant these discrepancies are, we computed the average difference between the RV obtained from UVES spectra and the RV obtained from GIRAFFE spectra for our targets, which is $-1.10 \pm 0.50 \text{ km s}^{-1}$ and becomes highly significant if looking at the velocity differences of targets FLD-121_100330 ($-2, 2 \text{ km s}^{-1}$, 4.4σ), FLD-121_100683 ($-2, 35 \text{ km s}^{-1}$, 4.7σ), FLD-121_100823 ($-2, 6 \text{ km s}^{-1}$, 5.2σ). These RV differences might be the result of some atmospheric jitter, a phenomenon causing such variations of RV consequently to the extended convective structure and other instabilities in RGB stars. In any case, the UVES spectra of our targets are characterised both by higher spectral resolution and wider spectral coverage in comparison to GIRAFFE ones, giving access to hopefully more precise CC RV estimates, with smaller uncertainties and based on more absorption lines.

3.4 Line selection

One of the most delicate tasks in the chemical analysis of stellar spectra is the identification of a set of unblended lines. The observed features can in fact be affected by different levels of blending with other unresolved or close transitions, leading to a spurious increase of the derived abundances. The level of blending depends on the strengths of each line, which is mainly driven by the stellar parameters, and on the spectral resolution of the adopted spectra. To evaluate the level of blending of each transition, we used the code K2 (developed by A. Mucciarelli at the Department of Physics & Astronomy of Bologna) to select the lines on a given synthetic spectrum. For each minimum of the synthetic spectrum, the dominant transition is recognized as well as other contaminating lines within a spectral region of 1.3 FWHM. For the dominant transition, the variation in abundance due to the overestimate of the line strength (because the depth of the minimum is also due to the other contaminating lines) is computed. We selected lines with

- individual transitions with variation of abundance smaller than 0.1 dex

- hyperfine/isotopic splitting
- precise laboratory oscillator strength $\log gf$, when possible

Since the level of blending for each transition depends also by the precise chemical mixture of the star, we adopted an iterative procedure:

1. a first line selection is performed adopting the abundances of the elements measured by Mucciarelli et al. (2023a) (for the elements not measured in that work, we adopted a solar-scaled pattern, $[X/Fe]=0$) and a first estimate of C and N abundances from molecular bands (this is done because several CN features can contaminate the red part of the spectra);
2. these lines are analysed with DAOSPEC/GALA to have a first (and rapid) estimate of all the abundances;
3. a new line selection is performed adopting synthetic spectra calculated with the entire array of abundances.

3.5 Preliminary analysis with DAOSPEC/GALA

We performed a preliminary chemical analysis using the codes DAOSPEC (Stetson & Pancino 2008) and GALA (Mucciarelli et al. 2013) and based on the measurement of the line equivalent width (EWs). DAOSPEC is a code that automatically normalises spectra using a polynomial fit and provides the EW for a list of lines, obtained through a Gaussian fitting, and the FWHM of the spectra (therefore an estimate of the observed spectral resolution). The measured EWs were then used to compute preliminary chemical abundances using the code GALA, which derives abundances matching observed and theoretical EWs. It is worth noting that this approach provides reliable abundances for unblended lines, but not for lines affected by hyperfine/isotopic splitting or blending with close transitions, or for lines where the continuum location is critical (i.e. close to molecular bands or in blue spectral region where the line density is high). Because the lines with splitting must be analysed using the spectral synthesis approach, we prefer to adopt the latter method for all the lines in order to avoid possible discrepancies in the continuum location between the two approaches. Nonetheless, the abundances derived with GALA provide a useful starting point for the following analysis based on spectral synthesis.

Some hundreds of lines were fitted in this process (~ 500 in each REDL spectra and less than 200 in each REDU spectra). We subsequently exploited the best fit FWHM values and saw the spectral resolution for the observed spectra from the DAOSPEC run resulted to be lower than $R=40,000$ (the instrumental resolution of the adopted slit configuration), since there are intrinsic and physical broadening effects acting on top of

the the dominant factor of instrumental broadening caused by the adopted UVES setting, causing it to roughly be $R=30,000$ in the gathered spectra. This lower resolution value was then used in the computation of new synthetic spectra, and new linelists for both REDL and REDU spectra have been created with the same Python script previously described, this time keeping only lines with EW larger than $15 \text{ m}\text{\AA}$. Before going on with the calculation of the chemical abundances of the single stars, these linelists were further examined and shortened through a visual inspection of the observed spectra of each star: we superimposed the synthetic spectra, together with marks reporting the wavelengths of any previously kept or discarded absorption feature, over the observed spectra of each star to ease the process of selecting only strong enough and unblended absorption lines. This visual inspection process eventually lead us to define a set of two linelists for each star, one for its REDL and one for its REDU spectrum.

3.6 Chemical abundances from spectral synthesis

The final computation of chemical abundances for all absorption lines was done using the SALVADOR code (developed by A. Mucciarelli at the Department of Physics & Astronomy of Bologna), which performs a χ^2 -minimisation between an observed spectrum and a series of synthetic spectra. For each star, we used as input the observed spectra after the global normalisation provided by the code DAOSPEC. Since this normalisation may present inaccuracies on smaller scales, these spectra were refined by interactively selecting a series of wavelength intervals of continuum emission from the comparison between observed spectra and appropriate synthetic models. Additionally, small refinements at the continuum location can be performed by applying multiplicative offsets to the spectrum. The synthetic spectra used in the SALVADOR code fits are computed on the fly in a spectral region of 5\AA around each absorption line, again through the SYNTH code, including all atomic and molecular lines from Kurucz/Castelli [line lists](#). The chemical mixture of these synthetic spectra are the abundances obtained from DAOSPEC/GALA. The adopted broadenings through convolution with Gaussian profile are such that the resolution in the synthetic spectra matches the resolution measured with DAOSPEC on the observed spectra.

All of the absorption lines fits have undergone a visual inspection, in order to remove bad fits or fits performed on clearly saturated lines, which are not sensitive to chemical abundance variations. An example of a good fit to an absorption line performed by SALVADOR is illustrated in [Figure 3.1](#). SALVADOR code has also been used for the computation of C and N abundances in each star, using Blue Arm setting spectra and performing fits over wider regions than the ones used for single absorption lines, since C and N abundances are measured off molecular absorption bands of CH and CN, respectively. Examples of CH and CN molecular band fits are showed in [Figures 3.2](#) and [3.3](#).

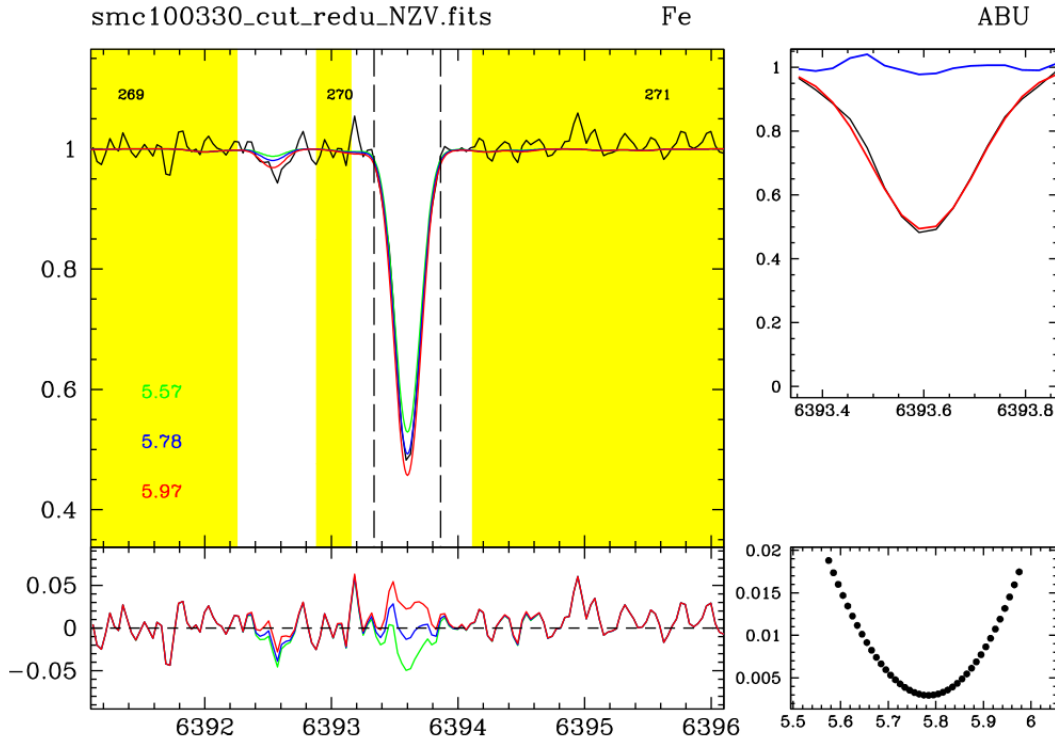


Figure 3.1: Example of a good fit output with the code SALVADOR on an isolated, not saturated, iron line in the REDU spectrum of the target FLD-121_100330. The plot on the left shows a 5\AA region around the fitted line, with the yellow regions showing the intervals selected to adjust the spectrum normalisation; beneath it, a plot with the residuals from the observed spectrum minus synthetic spectra (red, blue, green), with different abundances of the element of the fitted line, is reported for the same region. On the upper right, the best fit profile (red) is superimposed to the observed profile (black) of the line, along with the residuals (blue). The best fit is given by the abundance value corresponding to the minimum value of χ^2 , whose values for different abundances of the fitted element are reported in the lower right plot.

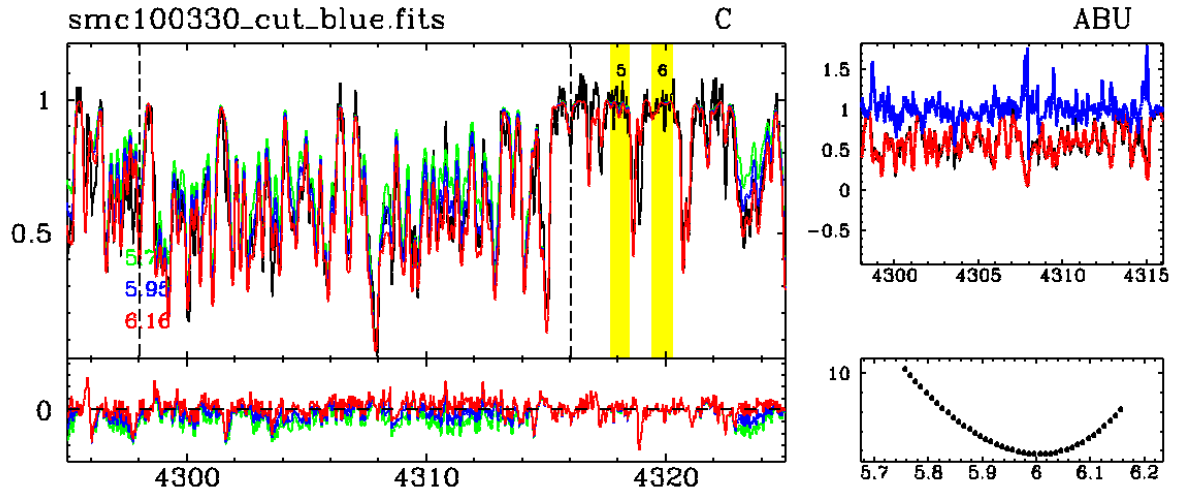


Figure 3.2: Example of a C abundance fit performed with the code SALVADOR on a CH molecular absorption band in the spectrum of the target FLD-121_100330, gathered with the UVES Blue Arm setting.

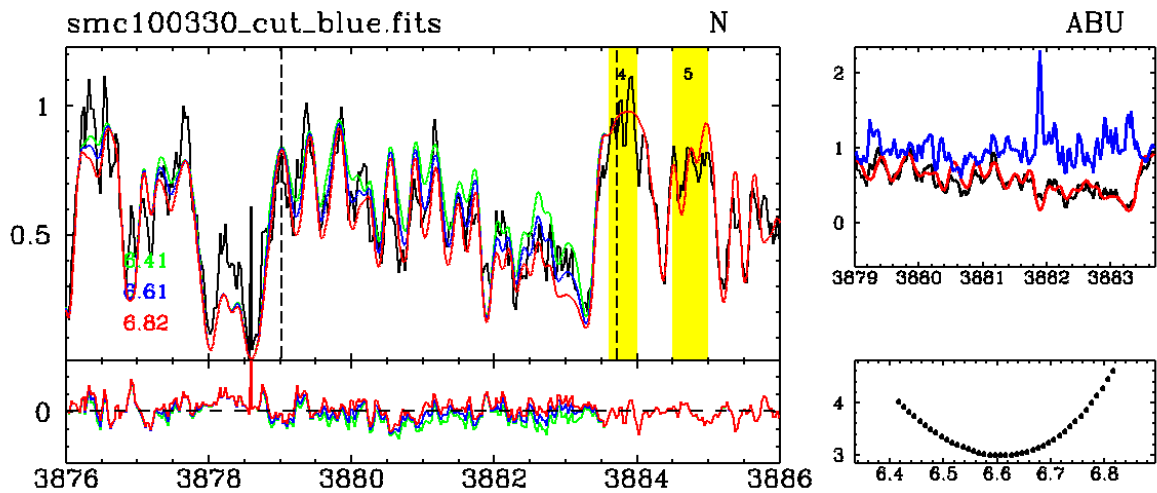


Figure 3.3: Example of a N abundance fit performed with the code SALVADOR on a CN molecular absorption band in the spectrum of the target FLD-121_100330, gathered with the UVES Blue Arm setting.

Once the value of the abundance minimising the discrepancy between the observed and the synthetic absorption line profile of an element is found, this value is saved as the abundance of that element deduced from that single absorption line. If more unblended and strong enough absorption lines of the same element are available in the observed spectrum of a star (and have consequently been reported in its linelists), the abundance values deduced from this process of χ^2 -minimisation are used in the computation of the average abundance of the X element, which is then normalised with respect to Fe and with respect to the solar content of X element itself, i.e. $[X/Fe]$. Solar reference abundances are from Grevesse & Sauval (1998), except for oxygen, for which we adopted the value by Caffau et al. (2011).

3.7 Uncertainties

The uncertainties in the computation of chemical abundances in our analysis are caused by measurement errors and by uncertainties from atmospheric parameters.

The average abundance value from multiple absorption lines of the same element in a given star comes with a measurement error, i.e. the abundance standard deviation normalised to the square root of the number of used absorption lines. These errors arise from the spectral fitting procedure (and are related to the SNR and resolution of the spectra), and from the $\log gf$ values assumed for each absorption feature. In the case only one absorption feature of an element is available, its abundance measurement error was measured by running a Monte Carlo simulation of 200 synthetic spectra with the addition of Poissonian noise to reproduce the observed SNR. The single feature was analysed in each of these spectra with SALVADOR, and the standard deviation of the derived abundance distribution is assumed as the measurement error.

The uncertainties arising from atmospheric parameters were computed with additional SALVADOR analyses in which atmospheric parameters were changed, according to their 1σ errors (50 K for T_{eff} , 0.1 for $\log g$, 0.2 km s⁻¹ for v_t), one at a time in order to evaluate the effect of each parameter uncertainty on the abundance computation.

These two sources of uncertainties were summed in quadrature to obtain the actual uncertainties associated to the measured abundances. Uncertainties in the measured iron abundances, $\sigma_{[Fe/H]}$, are therefore given by the following quadrature sum:

$$\sigma_{[Fe/H]} = \sqrt{\frac{\sigma_{Fe}^2}{N_{Fe}} + (\delta_{Fe}^{T_{eff}})^2 + (\delta_{Fe}^{\log g})^2 + (\delta_{Fe}^{v_t})^2}$$

For all the other elements, since we expressed the abundances in the form $[X/Fe]$, their uncertainties, $\sigma_{[X/Fe]}$, were consequently computed in the following way:

$$\sigma_{[X/Fe]} = \sqrt{\frac{\sigma_X^2}{N_X} + \frac{\sigma_{Fe}^2}{N_{Fe}} + (\delta_X^{Teff} - \delta_{Fe}^{Teff})^2 + (\delta_X^{\log g} - \delta_{Fe}^{\log g})^2 + (\delta_X^{vt} - \delta_{Fe}^{vt})^2}$$

In the two above formulas, σ_{Fe} and σ_X are the standard deviations of Fe and X element abundances, respectively; N_X and N_{Fe} are the number of fitted absorption lines used in the abundance measurement of Fe and the X element, respectively; $\delta_{X, Fe}^p$ are the abundance variations caused by the variation of the atmospheric parameter p .

3.8 NLTE corrections

The abundances of some chemical lines computed adopting the LTE approximation are known to be over/underestimated and non-LTE (NLTE) corrections are often required for these elements, especially in the case of metal-poor stars (Asplund 2005). In our analysis, we applied NLTE corrections by Alexeeva, Pakhomov, Mashonkina (2014) for Na I lines, by Mashonkina (2013) for Mg I lines, by Mashonkina et al. (2011) for Fe I lines, by Sitnova, Yakovleva, Belyaev, Mashonkina (2022) for Zn I line, by Mashonkina, Belyaev (2019) for Ba II lines, by Mashonkina, Gehren (2000) for Eu II line. All corrections were applied by means of the database from Mashonkina, Pakhomov, Sitnova et al. (2023). The Fe I NLTE corrections are all between +0.06 and +0.08 dex (except for target FLD-121_100823, which has +0.04 dex). Na I NLTE corrections are both negative and positive, but all within absolute values of 0.06 dex; the only exception is FLD-121_100330, with a -0.20 [Na/Fe] correction. The Mg I NLTE corrections overall determine a small [Mg/Fe] increase of +0.03 dex. Zn I has quite significant NLTE corrections between +0.09 and +0.15 dex, similarly to Eu II, whose NLTE corrections are between +0.09 and +0.13 dex, except for FLD-121_100330 and FLD-419_1355 +0.06 dex corrections.

Chapter 4

Results

Thanks to the high spectral resolution, the high SNR and the wide spectral coverage of the adopted UVES setting, we have been able to compute precise chemical abundances in the available sample of stars for 16 different chemical species: Fe, the light element Na, the α -elements O, Mg, Si, Ca, the iron-peak elements V, Mn, Ni, Zn, the s -process elements Cu, Y, Ba, La, Nd and the r -process element Eu. Some of them are lacking in the analysis by Mucciarelli et al. (2023a) due to spectral coverage and/or SNR (i.e. Mn, Zn, Eu) or only upper limits are provided, due to the spectral resolution (i.e. Na).

We will first show the chemical abundances we obtained for each of these elements or groups of elements, and display our sample in a series of $[X/Fe]$ - $[Fe/H]$ plots, showing also abundances of more metal rich SMC stars from Mucciarelli et al. (2023a). These abundance ratios were compared with those obtained for the MW reference star adopting the same assumptions in the chemical analysis and therefore removing most of the systematics of the analyses. This comparison allowed us to highlight the real difference between SMC and MW metal-poor stars of similar $[Fe/H]$. Additionally, we show abundance ratios for MW field stars from SAGA database. The comparison with the literature is affected by the systematics among the different analyses (in terms of model atmospheres, solar abundance values, NLTE corrections, line lists, and use of dwarf and giant stars). However, it is useful to display the overall trends in the MW based on a large number of stars. Generally, we found that our abundance ratios for the reference star BD06648 well agree with the average values of the literature MW stars at that $[Fe/H]$.

4.1 Iron

We measured between 120 and 150 unblended and strong enough Fe I lines across REDL and REDU spectra of each observed star. Given the high number of iron lines, we expect to get a solid and precise estimate of the iron abundance for the stars of our sample.

The derived $[\text{Fe}/\text{H}]$ are resumed in Table 4.1. We confirm that all the SMC stars are metal-poor, in the range of $[\text{Fe}/\text{H}]$ between -2.1 and -1.7 . According to the theoretical AMR of Pagel & Tautvaisiane (1998), these stars should have ages older than ~ 12 Gyr.

4.2 Carbon and Nitrogen

The Blue Arm CD2 390 UVES setting gives access to molecular absorption bands of CH and CN molecules, which were used to derive the C and N abundances in all the stars of the observed sample. A first computation of the C abundances was done based on the fitting of the CH molecular band at $\sim 4310\text{\AA}$. Then, the C abundances were fixed and the N abundances were computed by fitting the CN molecular bands at $\sim 3870\text{\AA}$ and $\sim 3880\text{\AA}$. After that, the N abundances were fixed and the C abundances were computed once more, and they confirmed to have their firstly computed values in all the observed stars.

As expected, since we are dealing with a sample of post RGB-bump stars, the abundances of C and N reflect the mixing effects occurring at the RGB bump (see e.g. Gratton et al. 2000): during the RGB phase, convective motions extending throughout the stellar structure bring towards the surface the material processed by thermonuclear reactions happening in the inner structure of the star, altering its chemical composition and the observed spectra. The effect of convection brings processed CNO material to the surface, causing a depletion of C and an increase of N during the RGB phase. All the stars of the sample actually show subsolar $[\text{C}/\text{Fe}]$ values and supersolar $[\text{N}/\text{Fe}]$ values, as it can be seen from Table 4.1. Blue Arm spectra of the selected MW star are not available, but we eventually assumed the average values from our SMC sample as a reference for its $[\text{C}/\text{Fe}]$ and $[\text{N}/\text{Fe}]$, since BD06648 is in the same RGB evolutionary stage as our SMC targets. The obtained values of C and N abundances were fixed in the subsequent computation of the abundances of all the other elements, including the iron abundance values computed above.

4.3 Sodium

Sodium is an odd- Z light element which is mainly synthesised during hydrostatic carbon burning in CC-SNe, and partially during hydrogen burning through the NeNa cycle and also in s -process (Clayton 2003). Also, the production of Na from massive stars is significantly dependent on the metallicity of the stars, at variance with the yields of α -elements that have a negligible dependence from $[\text{Fe}/\text{H}]$, thus making the interpretation of $[\text{Na}/\text{Fe}]$ abundance ratios difficult. The UVES spectra for our targets cover two Na I doublets, the first one at 5682.6\AA and 5688.2\AA , the second one being at 5890.0\AA and 5895.9\AA (Na D). However, the analysed targets often had very weak absorptions from the

first doublet, due to the low metallicity of the stars, and in these cases the Na abundances were determined only using the second doublet.

It is important to highlight that the Na D can have a chromospheric component, at variance with all the other lines used in this analysis that form in the photosphere. The model atmospheres adopted in this work include only photosphere and not chromosphere (which is very difficult to properly model). The majority of the stars brighter than $\log(L/L_{\odot}) \approx 2.7$ show the presence of active chromospheres (Mallia & Pagel 1981; Cacciari & Freeman 1983; Gratton et al. 1984; Cacciari et al. 2004; Meszaros et al. 2008). We checked that 5 out of 7 stars in our sample have emission on the wings of $H\alpha$, a typical diagnostic of chromosphere. Strong chromosphere can lead to core shift of the Na D lines, a shift we observed only for the star FLD-419_1355 (showing also the strongest Na D lines). The derived abundance ($[Na/Fe]=0.34$) is ~ 0.6 dex higher than the upper limit obtained from the other Na lines. For the other stars the doublet at 5682.6-5688.2Å provides Na abundances or upper limits compatible with those from Na D lines. Therefore we used Na from Na D lines for all the stars but FLD-419_1355 where we preferred the upper limits by the first doublet. NLTE $[Na/Fe]$ abundances are listed in Table 4.1.

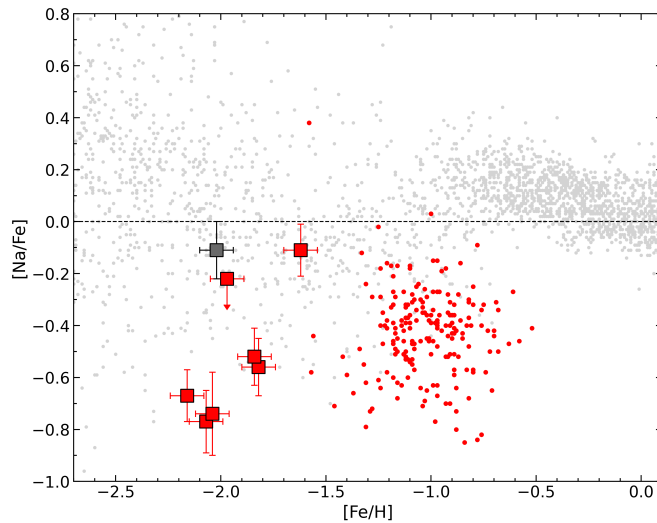


Figure 4.1: $[Na/Fe]$ abundances as function of $[Fe/H]$ for the analysed SMC (red squares) and MW (grey square) targets. $[Na/Fe]$ abundances for SMC stars from Mucciarelli et al. (2023a, red points) and for MW stars from SAGA database (grey points) in the range $-2.7 < [Fe/H] < +0.1$ are shown for comparison.

Overall, the measured sodium abundances are similar to the ones from MW stars in the same $[Fe/H]$ interval, as shown in Figure 4.1.

4.4 α -elements

The main site of production of α -elements are massive stars ending their evolution after few tens million years by exploding CC-SNe, while there is just a marginal contribution from SNe Ia explosions. The delay between the enrichment timescales of CC-SNe and SNe Ia explains the behaviour of $[\alpha/\text{Fe}]$ as a function of $[\text{Fe}/\text{H}]$ (Tinsley 1979; Matteucci & Greggio 1986). This characteristic chemical enrichment is observable in the well-known $[\alpha/\text{Fe}]$ - $[\text{Fe}/\text{H}]$ plot.

In the first phases of chemical enrichment of a galaxy, short-lived massive stars exploding as CC SNe from multiple stellar generations follow one another, filling the gas of their host galaxy with a constant value, a plateau of $[\alpha/\text{Fe}]$ abundance and slowly increasing $[\text{Fe}/\text{H}]$. The level of the $[\alpha/\text{Fe}]$ plateau and the metallicity at which $[\alpha/\text{Fe}]$ starts to decrease are useful information to reconstruct the past SF activity and the initial mass function of a galaxy. On the other hand, even though the SNe Ia from the most massive stars that end their evolution in such a way happen just after few tens million years (right after a first generation of CC SNe explosions), the contribution of this class of SNe to chemical enrichment becomes relevant only after some hundred million years or even after ~ 1 Gyr. Once the contribution from the enrichment of SNe Ia becomes relevant, a decrease of $[\alpha/\text{Fe}]$ from the initial plateau is generally observed above a certain value of $[\text{Fe}/\text{H}]$, as a consequence of the great iron-peak elements and small α -element production from SNe Ia: this is the main feature of the $[\alpha/\text{Fe}]$ - $[\text{Fe}/\text{H}]$ plot, and it is commonly referred to as the α -knee, a fundamental characteristic in reconstructing the SFR and SF efficiency and chemical evolution of a stellar system. The lower is the SF efficiency of a galaxy, the lower would be the $[\text{Fe}/\text{H}]$ corresponding to the position of the α -knee.

Oxygen: oxygen is the third most abundant element in the Universe after hydrogen and helium: it is an α -element mainly produced during the hydrostatic burning of He, C and Ne in massive stars (with a peak of efficiency around $30 - 35 M_{\odot}$), while no contribution is expected from SNe Ia. An underabundance of oxygen may indeed indicate a lower contribution to chemical enrichment from massive stars exploding as CC SNe. The oxygen abundances of our targets have been computed from the 6300.3\AA O I absorption line, the only oxygen absorption feature available throughout the used UVES setting. The abundance values measured for $[\text{O}/\text{Fe}]$ are reported in Table 4.2.

The seven stars of our sample have enhanced $[\text{O}/\text{Fe}]$ but lower than the typical values observed among the Galactic stars, as shown in Figure 4.2.

Magnesium: magnesium is a hydrostatic α -element, mainly produced from hydrostatic carbon burning and explosive neon burning in massive stars; as for oxygen, no contribution is expected from SNe Ia and a magnesium underabundance may indicate a lower contribution to chemical enrichment from stars in this mass range, which are exploding as CC SNe. The magnesium abundances for our targets have been computed from a sample of three Mg I absorption features in the REDL spectra: the absorption

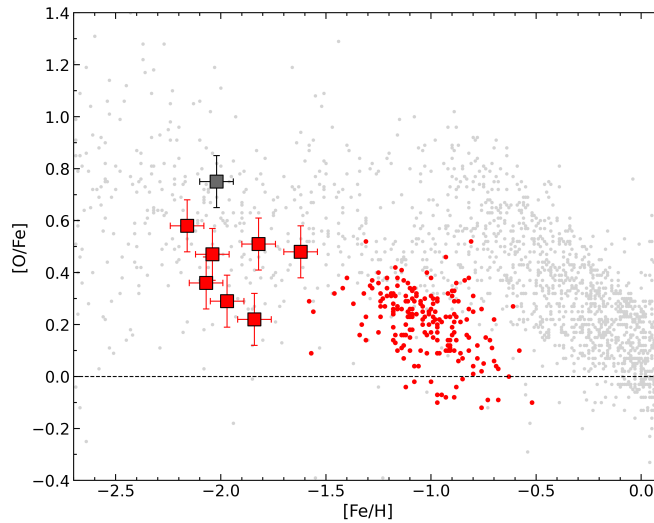


Figure 4.2: $[O/Fe]$ abundances as function of $[Fe/H]$ for the analysed SMC (red squares) and MW (grey square) targets. $[O/Fe]$ abundances for SMC stars from Mucciarelli et al. (2023a, red points) and for MW stars from SAGA database (grey points) in the range $-2.7 < [Fe/H] < +0.1$ are shown for comparison.

lines at 5172.7\AA and 5183.6\AA (belonging to the Mg b triplet) and the absorption line at 5711.1\AA . The $[Mg/Fe]$ abundances computed from UVES spectra are summarised in Table 4.2.

When plotted against $[Fe/H]$, our targets are enriched in $[Mg/Fe]$ but lower than the MW reference stars. The measured abundances, plotted in Figure 4.3 align along a trend of decreasing $[Mg/Fe]$ for increasing $[Fe/H]$, apart from the metal richer FLD-121_100823, which confirms a decrease in $[Mg/Fe]$ happening at lower $[Fe/H]$ values with respect to the MW.

Silicon: silicon is an explosive α -element and it is produced mainly during explosive oxygen burning in massive stars (with a peak of efficiency around $15 - 25 M_{\odot}$), with a small, though not negligible, contribution from SNe Ia (Romano et al. 2010, Kobayashi et al. 2020). Our UVES spectra include just one unblended Si absorption feature at 5948.5\AA (and another absorption line at 6155.1\AA just for FLD-121_100823), from which we computed the Si abundances of our stars, reported in Table 4.2.

When plotted against $[Fe/H]$ (Figure 4.4), $[Si/Fe]$ abundances show a similar behaviour to that of $[Mg/Fe]$, with a slightly steeper decreasing $[Si/Fe]$ trend for increasing $[Fe/H]$, and a higher value for the metal richer target FLD-121_100823. Just as magnesium, silicon abundance drops to lower values at lower $[Fe/H]$ than in the MW.

Calcium: calcium is an explosive α -element mainly produced during incomplete silicon and oxygen burning in massive stars in the range $15 - 25 M_{\odot}$, with a small non negligible contribution from SNe Ia. The Ca abundances for our sample of stars have

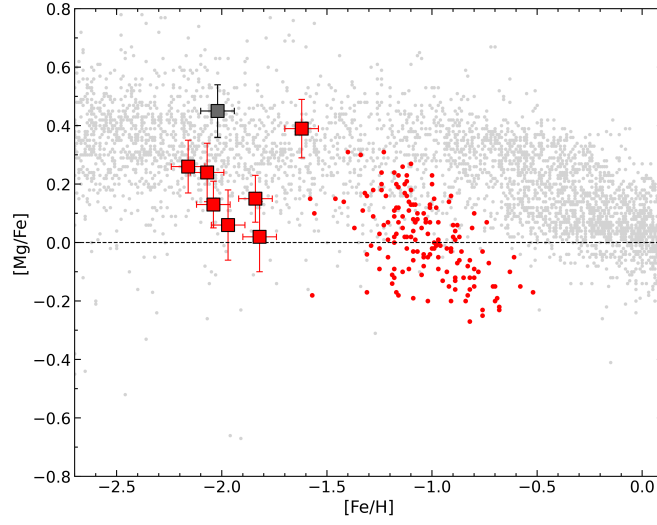


Figure 4.3: $[\text{Mg}/\text{Fe}]$ abundances as function of $[\text{Fe}/\text{H}]$ for the analysed SMC (red squares) and MW (grey square) targets. $[\text{Mg}/\text{Fe}]$ abundances for SMC stars from Mucciarelli et al. (2023a, red points) and for MW stars from SAGA database (grey points) in the range $-2.7 < [\text{Fe}/\text{H}] < +0.1$ are shown for comparison.

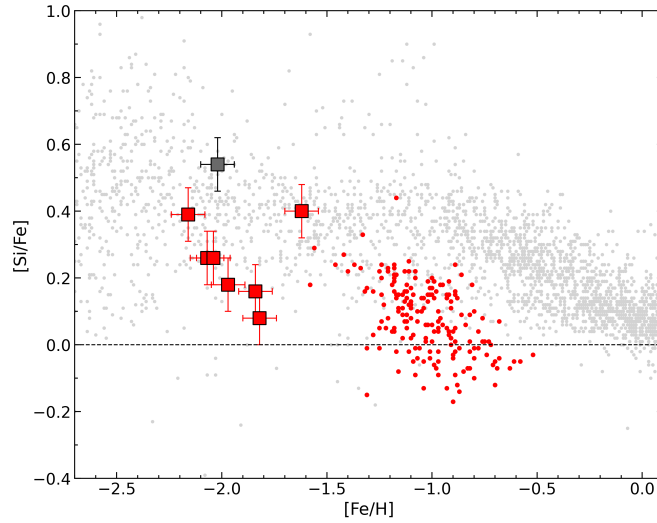


Figure 4.4: $[\text{Si}/\text{Fe}]$ abundances as function of $[\text{Fe}/\text{H}]$ for the analysed SMC (red squares) and MW (grey square) targets. $[\text{Si}/\text{Fe}]$ abundances for SMC stars from Mucciarelli et al. (2023a, red points) and for MW stars from SAGA database (grey points) in the range $-2.7 < [\text{Fe}/\text{H}] < +0.1$ are shown for comparison.

been computed based on 15 or more clear absorption lines throughout the REDL and REDU spectra. $[\text{Ca}/\text{Fe}]$ abundances are reported in Table 4.2.

The $[\text{Ca}/\text{Fe}]-[\text{Fe}/\text{H}]$ plot in Figure 4.5 displays the differences in $[\text{Ca}/\text{Fe}]$ between the SMC and the MW at different $[\text{Fe}/\text{H}]$. Our targets show a decreasing trend of $[\text{Ca}/\text{Fe}]$ for increasing $[\text{Fe}/\text{H}]$, with FLD-121_100823 exhibiting a higher $[\text{Ca}/\text{Fe}]$. This drop in calcium abundance happens at lower $[\text{Fe}/\text{H}]$ than in the MW, just as for the other α -elements analysed.

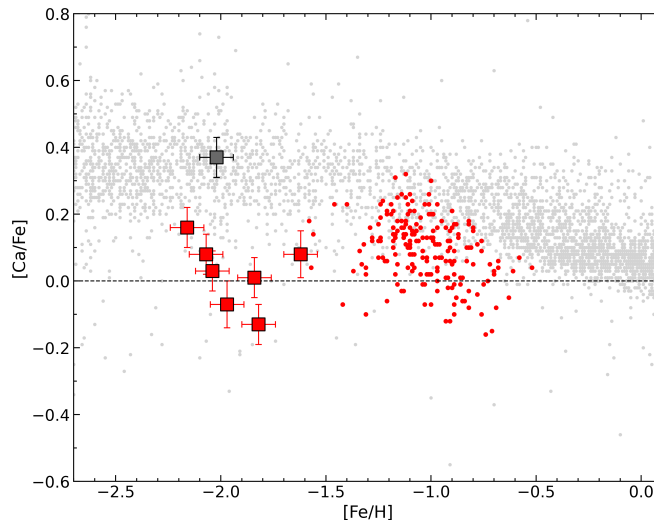


Figure 4.5: $[\text{Ca}/\text{Fe}]$ abundances as function of $[\text{Fe}/\text{H}]$ for the analysed SMC (red squares) and MW (grey square) targets. $[\text{Ca}/\text{Fe}]$ abundances for SMC stars from Mucciarelli et al. (2023a, red points) and for MW stars from SAGA database (grey points) in the range $-2.7 < [\text{Fe}/\text{H}] < +0.1$ are shown for comparison.

4.5 Iron-peak elements

Iron-peak elements are produced through different nucleosynthesis paths and ejected in the interstellar medium by different classes and types of supernovae. Among with CC SNe, there is also some relevant enrichment coming from hypernovae (HNe), which are supernovae explosions with at least an order of magnitude larger explosion energy than those of standard CC SNe and are generally associated with stars as massive as $30 - 35 M_{\odot}$. Some amount of the iron-peak elements is supplied by an important SNe Ia contribution, which even become the dominant one on longer timescales. The interplay between the different classes and types of supernovae in producing different iron-peak elements with different yields and proportions is at the basis of different chemical enrichments over time for these iron-peak elements.

Vanadium: vanadium is mainly produced by incomplete explosive Si burning in massive stars, but a small contribution by SNe Ia is expected as well. Vanadium abundance

tends to decrease with increasing $[\text{Fe}/\text{H}]$ as the result of delayed relevant contribution to iron enrichment provided by SNe Ia. Few unblended absorption lines, between 3 and 9 depending on the studied star, are retrievable from the observed UVES spectra. The derived values of $[\text{V}/\text{Fe}]$ abundances are summed up in Table 4.3

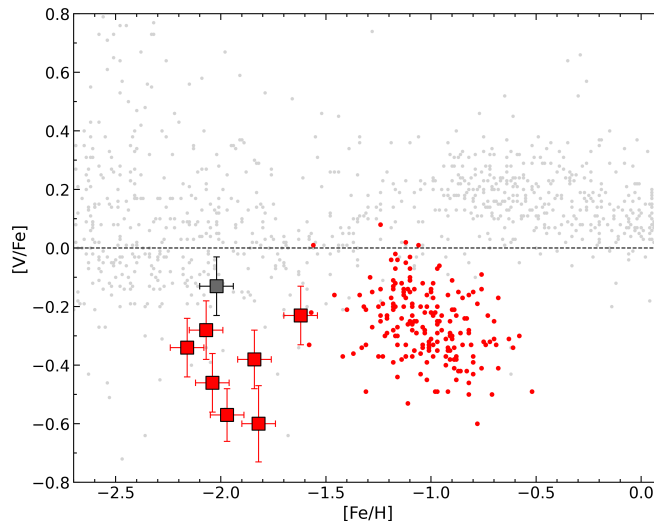


Figure 4.6: $[\text{V}/\text{Fe}]$ abundances as function of $[\text{Fe}/\text{H}]$ for the analysed SMC (red squares) and MW (grey square) targets. $[\text{V}/\text{Fe}]$ abundances for SMC stars from Mucciarelli et al. (2023a, red points) and for MW stars from SAGA database (grey points) in the range $-2.7 < [\text{Fe}/\text{H}] < +0.1$ are shown for comparison.

The abundances of vanadium from the analysed metal-poor SMC stars are lower than the typical $[\text{V}/\text{Fe}]$ abundances at similar $[\text{Fe}/\text{H}]$ a discrepancy which is preserved also in more metal rich stars, as it can be seen from Figure 4.6.

Manganese: manganese is almost totally produced in SN Ia with a negligible contribution by massive stars. In the Galaxy, $[\text{Mn}/\text{Fe}]$ is subsolar until $[\text{Fe}/\text{H}] \sim -1$ where the contribution of SNe Ia starts to dominate, increasing $[\text{Mn}/\text{Fe}]$. This iron-peak element is indeed known to be mostly produced by SNe Ia, and its yields are also expected to increase with the metallicity of the SN Ia progenitor and being dependent on the explosion mechanism of the SNe Ia. At higher metallicities, when the contribution by SNe Ia significantly increases and becomes dominant, the abundance of Mn seems to increase, but some observation of low manganese abundances even at high metallicities suggest its enrichment may be dominated by metal-poor SNe Ia. For each of the stars observed with UVES, the manganese abundances were computed based on between 2 and 5 unblended absorption lines. The values obtained for $[\text{Mn}/\text{Fe}]$ are shown in Table 4.3.

The analysed targets were compared with MW stars in a $[\text{Mn}/\text{Fe}]$ - $[\text{Fe}/\text{H}]$ plot, shown hereafter in Figure 4.7: manganese abundances from the sample of metal-poor SMC stars are substantially aligned with the ones of MW stars in the same range of $[\text{Fe}/\text{H}]$.

Also for this element, the most metal-rich star of the sample (FLD-121_100823) shows a different behaviour with a lower $[\text{Mn}/\text{Fe}]$.

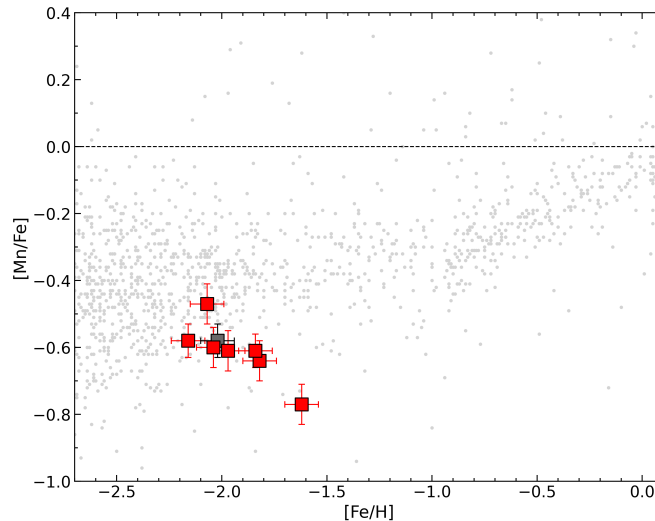


Figure 4.7: $[\text{Mn}/\text{Fe}]$ abundances as function of $[\text{Fe}/\text{H}]$ for the analysed SMC (red squares) and MW (grey square) targets. $[\text{Mn}/\text{Fe}]$ abundances for MW stars from SAGA database (grey points) in the range $-2.7 < [\text{Fe}/\text{H}] < +0.1$ are shown for comparison.

Nichel: nichel is an iron-peak element largely produced by SNe Ia, in the zones undergoing complete explosive Si burning in stars, and also partially produced in CC SNe explosions. Since its nucleosynthesis shares similarities with iron one, nichel can in fact trace iron chemical evolution. The decrease of nichel abundances in stars with progressively lower iron content suggests a increasingly lower contribution by sub-Chandrasekhar mass SNe Ia. Nichel is the second element in terms of number of unblended absorption features in our sample of stellar spectra, directly after iron: there are between 30 and 50 clearly visible and unblended Ni I absorption lines, from which we have been able to hopefully draw solid estimates of nichel abundances, summarised in Table 4.3.

The subsolar values measured for nichel abundances seem to be aligned along a decreasing trend in the $[\text{Ni}/\text{Fe}]$ - $[\text{Fe}/\text{H}]$ plot shown in Figure 4.8. On top of that, the SMC metal-poor stars seem to be slightly underabundant in nichel with respect to MW stars at similar $[\text{Fe}/\text{H}]$.

Zinc: zinc is characterised by a pretty peculiar nucleosynthesis with respect to the iron-peak elements previously discussed in this section. Zinc is in fact almost completely produced by stars that end their evolution as HNe. Therefore, any measurement of zinc abundances in stars belonging to a specific galaxy may offer crucial information on HNe and high-mass stars rates and contribution to the chemical enrichment of that specific galaxy. As a rule of thumb, a lower zinc abundance value indicates a lower contribution by massive stars, in particular by HNe, to chemical enrichment of the gas of a galaxy.

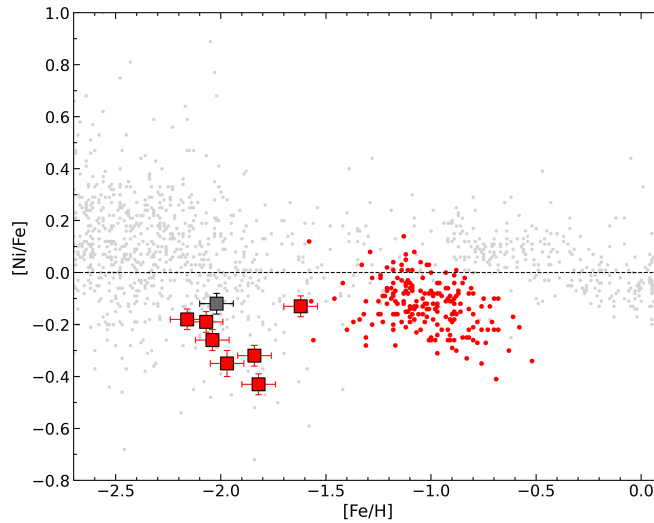


Figure 4.8: $[\text{Ni}/\text{Fe}]$ abundances as function of $[\text{Fe}/\text{H}]$ for the analysed SMC (red squares) and MW (grey square) targets. $[\text{Ni}/\text{Fe}]$ abundances for SMC stars from Mucciarelli et al. (2023a, red points) and for MW stars from SAGA database (grey points) in the range $-2.7 < [\text{Fe}/\text{H}] < +0.1$ are shown for comparison.

The only observable absorption line in the UVES spectra of our sample is the Zn I line located at a wavelength of 4810.5\AA , and it was observed in each of the targets. The measured zinc abundances are summarised in Table 4.3.

The $[\text{Zn}/\text{Fe}]-[\text{Fe}/\text{H}]$ plot shown in Figure 4.9 hints at a slight underabundance of zinc in the analysed SMC targets with respect to metal-poor MW stars, which could be caused by a smaller contribution of HNe to the early chemical enrichment of the SMC with respect to the MW.

4.6 r -process elements

The rapid neutron capture processes, also known as r -processes, occur in the presence of a very high neutron flux ($> 10^{20}$ neutron cm^{-3}), which allows seed nuclei to capture several neutrons one after the other, and only afterwards undergo a series of β decays which transform them into stable nuclei. Several sites of production of r -process elements have been proposed, such as neutron-star mergers (Lattimer & Schramm 1974), collapsars (Siegel et al. 2019) and proto-magnetars (Nishimura et al. 2015). Some chemical evolution models that include neutron-star mergers as the only r -process source have been developed, but those models are not able to reproduce the Galactic distribution of r -process elements (Molero et al. 2021)

When it comes to the observation of spectral features from r -process elements, eu-

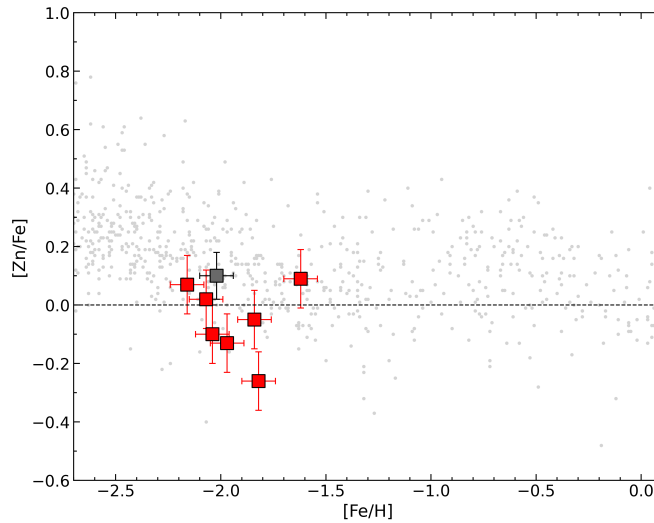


Figure 4.9: $[\text{Zn}/\text{Fe}]$ abundances as function of $[\text{Fe}/\text{H}]$ for the analysed SMC (red squares) and MW (grey square) targets. $[\text{Zn}/\text{Fe}]$ abundances for MW stars from SAGA database (grey points) in the range $-2.7 < [\text{Fe}/\text{H}] < +0.1$ are shown for comparison.

europium is the most easily observed element thought to be produced exclusively through the r -process. High europium abundances can be interpreted as the evidence of a very efficient r -process element production. Moreover, a constant $[\text{Eu}/\text{Fe}]$ at different metallicities may be indicative of similar Eu and Fe synthesis timescales. In the Galaxy, $[\text{Eu}/\text{Fe}]$ exhibits a clear behaviour, with enhanced values in metal-poor stars ($[\text{Fe}/\text{H}] < -1$) and a large scatter, and a decrease at higher metallicity. The decrease of $[\text{Eu}/\text{Fe}]$ can be easily explained within the standard time delay model used to explain the decline of $[\alpha/\text{Fe}]$. In fact, SNe Ia do not produce r -process elements. Another interesting feature observed in the Galactic stars is the large star-to-star scatter among the metal-poor stars, likely due to the rarity of these events. In our sample of SMC stars, we computed europium abundances from the EW of the Eu II absorption line at 6645.1Å. The NLTE $[\text{Eu}/\text{Fe}]$ abundances are summarised in Table 4.5.

In the $[\text{Eu}/\text{Fe}]$ - $[\text{Fe}/\text{H}]$ plot (Figure 4.10), the $[\text{Eu}/\text{Fe}]$ measured for our sample are indeed comparable with Galactic stars europium content. The SMC targets exhibit a large star-to-star scatter in $[\text{Eu}/\text{Fe}]$ larger than the typical uncertainties, which indicates an intrinsic scatter among the stars. In particular, most of the stars are enhanced in $[\text{Eu}/\text{Fe}]$, with the case of FLD-121_100330 reaching $[\text{Eu}/\text{Fe}] = +1.05$, while the star FLD-419_1355 has a very low Eu abundance, and we provide only an upper limit due to the weakness of the measured Eu II transition.

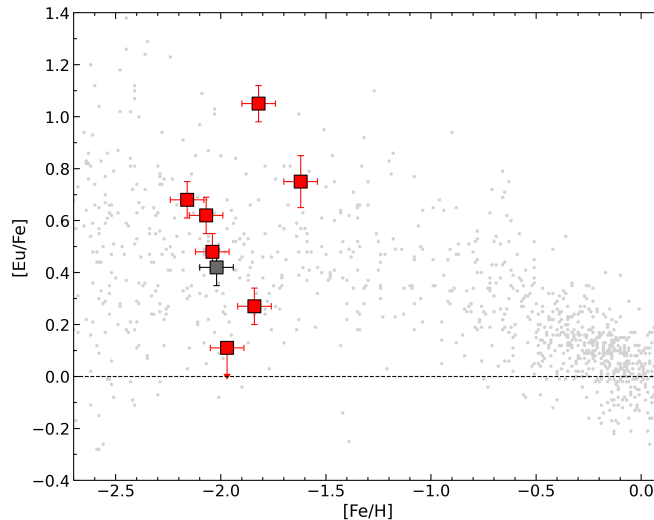


Figure 4.10: $[\text{Eu}/\text{Fe}]$ abundances as function of $[\text{Fe}/\text{H}]$ for the analysed SMC (red squares) and MW (grey square) targets. $[\text{Eu}/\text{Fe}]$ abundances for MW stars from SAGA database (grey points) in the range $-2.7 < [\text{Fe}/\text{H}] < +0.1$ are shown for comparison.

4.7 *s*-process elements

The slow neutron capture process (also known as *s*-process) elements are heavier than the iron-peak group elements and are produced through slow neutron-capture processes on seed nuclei, which are then followed by β decays. A source of neutrons is required for the *s*-process ($10^7 - 10^{12}$ neutrons cm^{-3}). Some elements heavier than iron-peak elements are mainly produced through *s*-processes happening in AGB stars. A considerable enhancement of *s*-process elements might indeed be due to mass transfer processes from AGB companion stars in binary systems. It is possible to distinguish between light and heavy *s*-process elements, depending on their atomic number. The ratio of heavy-to-light *s*-process elements is indeed sensitive to metallicity: when the metallicity of an AGB star is higher, the production of light *s*-process elements is favoured over heavy ones. This happens because at higher metallicities a larger number of seed nuclei for *s*-process element formation is available and, assuming the neutron flux is constant with $[\text{Fe}/\text{H}]$, those neutrons are then captured by more seed nuclei during the *s*-process, creating a great amount of light *s*-process elements and just few heavy *s*-process elements.

Copper: copper is mainly produced in massive stars during core-helium and carbon-shell hydrostatic burnings, as well as in explosive complete Ne burning (Romano & Matteucci 2007). On the top of that, there is a small contribution by AGB stars and a rather negligible contribution by SNe Ia. The yields of copper are expected to increase with growing metallicity, since the weak *s*-process taking place in massive stars becomes increasingly important at higher metallicities. A lower copper abundance may indicate a

lower contribution to the chemical enrichment by massive stars in the observed system. The copper abundances of our targets were computed after the 5105.6Å Cu I absorption line, which was clearly observable in each spectrum of our sample. The obtained [Cu/Fe] abundances are reported in Table 4.4.

The [Cu/Fe]-[Fe/H] plot of Figure 4.11 shows how the [Cu/Fe] abundances measured for our targets are comparable with those of MW stars, while a quite evident discrepancy emerged at higher [Fe/H] values between stars of the SMC and of the MW from the analysis of Mucciarelli et al. (2023a).

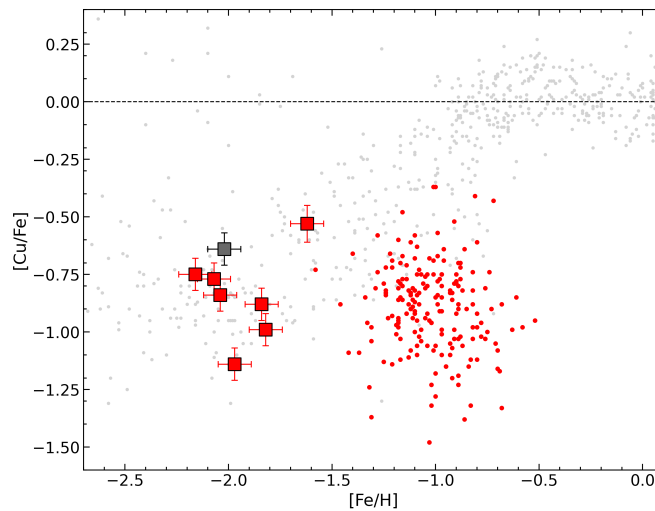


Figure 4.11: [Cu/Fe] abundances as function of [Fe/H] for the analysed SMC (red squares) and MW (grey square) targets. [Cu/Fe] abundances for SMC stars from Mucciarelli et al. (2023a, red points) and for MW stars from SAGA database (grey points) in the range $-2.7 < [\text{Fe}/\text{H}] < +0.1$ are shown for comparison.

Yttrium: yttrium is a light *s*-process element produced by AGB stars over a large mass range. In our sample of observations, between 5 and 11 unblended yttrium absorption lines were identified for each star. The yttrium abundances computed for the studied sample are summarised in Table 4.4.

Figure 4.12 shows the abundances of the analysed SMC stars in a [Y/Fe]-[Fe/H] plot: their values are lower than a large fraction of MW stars of similar [Fe/H].

Barium: barium is a heavy *s*-process element produced in low-mass, generally below $4 M_{\odot}$, AGB stars, with yields highly dependent on metallicities, and in a minor amount in more massive stars. At lower metallicities, barium is also formed through rapid neutron capture processes that occur in rare and energetic events, such as neutron star mergers or collapsars. High barium abundances may be an indicator of a galaxy-wide initial mass function (IMF) biased in favour of low-mass stars and suggest a very efficient production mechanism of *s*-process elements is in place in the observed environment. The barium

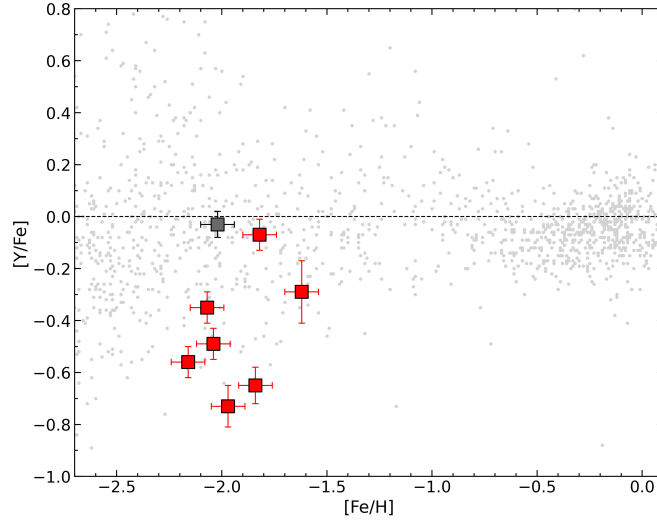


Figure 4.12: $[Y/Fe]$ abundances as function of $[Fe/H]$ for the analysed SMC (red squares) and MW (grey square) targets. $[Y/Fe]$ abundances for MW stars from SAGA database (grey points) in the range $-2.7 < [Fe/H] < +0.1$ are shown for comparison.

abundances measured in our targets are based on the analysis of the Ba II absorption lines at 5853.7\AA , 6141.7\AA , 6496.9\AA , and their are shown in Table 4.4.

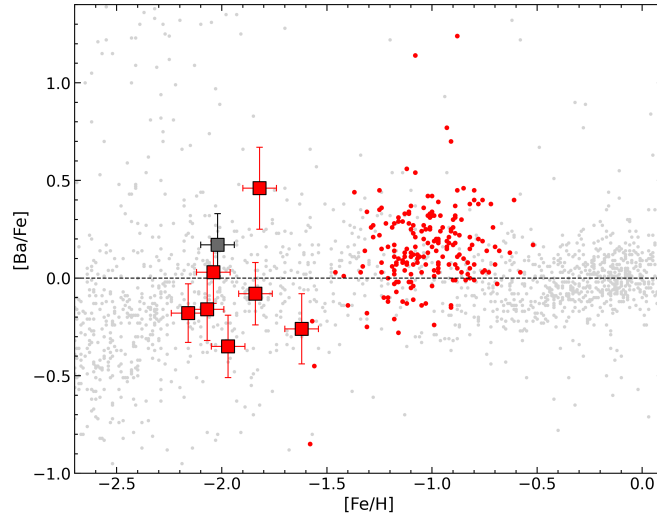


Figure 4.13: $[Ba/Fe]$ abundances as function of $[Fe/H]$ for the analysed SMC (red squares) and MW (grey square) targets. $[Ba/Fe]$ abundances for SMC stars from Mucciarelli et al. (2023a, red points) and for MW stars from SAGA database (grey points) in the range $-2.7 < [Fe/H] < +0.1$ are shown for comparison.

The [Ba/Fe]-[Fe/H] plot (Figure 4.13) highlights how the sample of SMC metal-poor stars has [Ba/Fe] comparable with Galactic values. However, the target FLD-121_100330 stands out from the others and is sensibly higher in [Ba/Fe] than Galactic stars as well.

Lanthanum: lanthanum, just as barium, is a heavy *s*-process element produced in low-mass, generally below $4 M_{\odot}$, AGB stars, with yields highly dependent on metallicities, and in a minor amount in more massive stars. Similarly to barium, lanthanum is formed, at low metallicities, through rapid processes that occurring in neutron star mergers or collapsars, and high lanthanum abundances may be correlated to a bottom-heavy IMF and a very efficient *s*-process elements production. Plenty of lanthanum unblended absorption lines were available in our observed spectra, but only few of them were strong enough to be analysed in all the stars of our sample, from a minimum of 2 to a maximum of 18 in the case of stars with larger abundances of *s*-process elements. The [La/Fe] abundances for our sample are reported in Table 4.4.

Similarly to barium, the [La/Fe]-[Fe/H] plot (Figure 4.14) highlights how the sample of SMC metal-poor stars has [La/Fe] comparable with Galactic values. Once more, the target FLD-121_100330 has sensibly higher [La/Fe] with respect to other SMC metal-poor stars, and with respect to Galactic stars as well.

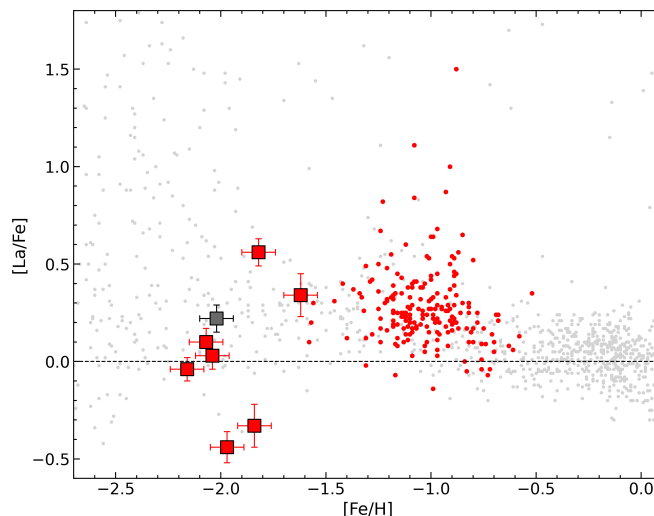


Figure 4.14: [La/Fe] abundances as function of [Fe/H] for the analysed SMC (red squares) and MW (grey square) targets. [La/Fe] abundances for SMC stars from Mucciarelli et al. (2023a, red points) and for MW stars from SAGA database (grey points) in the range $-2.7 < [\text{Fe}/\text{H}] < +0.1$ are shown for comparison.

Neodymium: neodymium is a heavy *s*-process element which is produced by low-mass ($< 4 M_{\odot}$) AGB stars, but is also known to be equally produced by rapid neutron capture processes. Throughout the analysis UVES spectra, neodymium is the most frequent *s*-process element in terms of number of observable absorption lines. The abun-

dance values computed for Nd are based on 3 to 18 absorption lines. Table 4.5 shows the neodymium abundances we obtained.

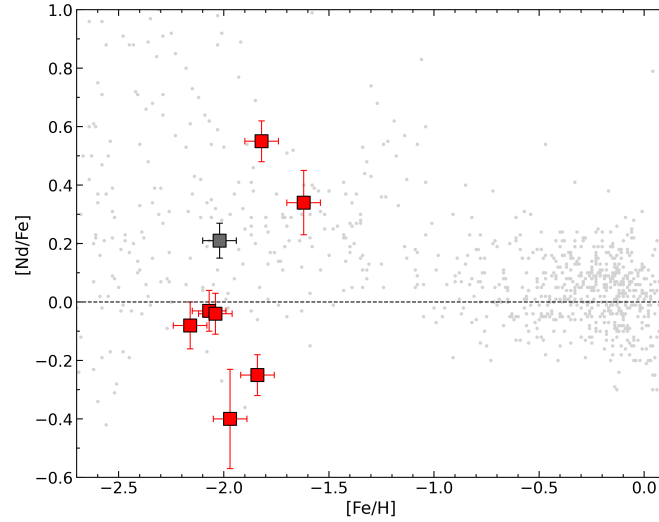


Figure 4.15: $[\text{Nd}/\text{Fe}]$ abundances as function of $[\text{Fe}/\text{H}]$ for the analysed SMC (red squares) and MW (grey square) targets. $[\text{Nd}/\text{Fe}]$ abundances for MW stars from SAGA database (grey points) in the range $-2.7 < [\text{Fe}/\text{H}] < +0.1$ are shown for comparison.

The obtained $[\text{Nd}/\text{Fe}]$ abundances are generally lower than Galactic stars (Figure 4.15 for our targets, except for FLD-121_100330 and FLD-121_100823, which are consistently supersolar).

In conclusion, we note as several s -process elements exhibit the same star-to-star scatter observed for $[\text{Eu}/\text{Fe}]$ and in particular the most r -rich star (FLD-121_100330) is high also in s -process elements, while the two stars with lower $[\text{Eu}/\text{Fe}]$ are lower also in s -process elements. This suggests that at these metallicities, where the AGB stars have not contributed to enrich the gas, the production of the so-called s -process elements is mainly due to r -processes.

Target	[Fe/H]	[C/Fe]	[N/Fe]	[Na/Fe]
FLD-121_100330	-1.82 ± 0.08	-0.71 ± 0.12	$+0.43 \pm 0.07$	-0.56 ± 0.11
FLD-121_100514	-2.16 ± 0.08	-1.24 ± 0.12	$+0.71 \pm 0.07$	-0.67 ± 0.10
FLD-121_100683	-2.07 ± 0.08	-1.05 ± 0.12	$+0.43 \pm 0.07$	-0.77 ± 0.12
FLD-121_100767	-1.84 ± 0.08	-1.14 ± 0.12	$+0.37 \pm 0.07$	-0.52 ± 0.11
FLD-121_100781	-2.04 ± 0.08	-1.21 ± 0.12	$+0.35 \pm 0.07$	-0.75 ± 0.16
FLD-121_100823	-1.62 ± 0.08	-0.82 ± 0.12	$+0.22 \pm 0.07$	-0.11 ± 0.10
FLD-419_1355	-1.97 ± 0.08	-1.00 ± 0.12	$+0.45 \pm 0.07$	< -0.22
BD06448 (MW)	-2.02 ± 0.08			-0.11 ± 0.11

Table 4.1: [Fe/H], [C/Fe], [N/Fe] and [Na/Fe] abundances of SMC and MW targets of our study. The abundances reported without errors and with the < sign are upper limit estimates.

Target	[O/Fe]	[Mg/Fe]	[Si/Fe]	[Ca/Fe]
FLD-121_100330	$+0.51 \pm 0.10$	$+0.02 \pm 0.12$	$+0.08 \pm 0.08$	-0.13 ± 0.06
FLD-121_100514	$+0.58 \pm 0.10$	$+0.26 \pm 0.09$	$+0.39 \pm 0.08$	$+0.16 \pm 0.06$
FLD-121_100683	$+0.36 \pm 0.10$	$+0.24 \pm 0.10$	$+0.26 \pm 0.08$	$+0.08 \pm 0.06$
FLD-121_100767	$+0.22 \pm 0.10$	$+0.15 \pm 0.08$	$+0.16 \pm 0.08$	$+0.01 \pm 0.06$
FLD-121_100781	$+0.47 \pm 0.10$	$+0.13 \pm 0.08$	$+0.26 \pm 0.08$	$+0.03 \pm 0.06$
FLD-121_100823	$+0.48 \pm 0.10$	$+0.39 \pm 0.10$	$+0.40 \pm 0.08$	$+0.08 \pm 0.07$
FLD-419_1355	$+0.29 \pm 0.10$	$+0.06 \pm 0.12$	$+0.18 \pm 0.08$	-0.07 ± 0.07
BD06448 (MW)	$+0.75 \pm 0.10$	$+0.45 \pm 0.09$	$+0.54 \pm 0.08$	$+0.37 \pm 0.06$

Table 4.2: [O/Fe], [Mg/Fe], [Si/Fe] and [Ca/Fe] abundances of SMC and MW targets of our study.

Target	[V/Fe]	[Mn/Fe]	[Ni/Fe]	[Zn/Fe]
FLD-121_100330	-0.60 ± 0.13	-0.64 ± 0.06	-0.43 ± 0.08	-0.26 ± 0.10
FLD-121_100514	-0.34 ± 0.10	-0.58 ± 0.05	-0.18 ± 0.08	$+0.07 \pm 0.10$
FLD-121_100683	-0.28 ± 0.10	-0.47 ± 0.06	-0.19 ± 0.08	$+0.02 \pm 0.10$
FLD-121_100767	-0.38 ± 0.10	-0.61 ± 0.05	-0.32 ± 0.08	-0.05 ± 0.10
FLD-121_100781	-0.46 ± 0.10	-0.60 ± 0.06	-0.26 ± 0.08	-0.10 ± 0.10
FLD-121_100823	-0.23 ± 0.10	-0.77 ± 0.05	-0.13 ± 0.08	$+0.09 \pm 0.10$
FLD-419_1355	-0.57 ± 0.09	-0.61 ± 0.06	-0.35 ± 0.05	-0.13 ± 0.10
BD06448 (MW)	-0.13 ± 0.10	-0.58 ± 0.05	-0.12 ± 0.04	$+0.10 \pm 0.08$

Table 4.3: [V/Fe], [Mn/Fe], [Ni/Fe] and [Zn/Fe] abundances of SMC and MW targets of our study.

Target	[Cu/Fe]	[Y/Fe]	[Ba/Fe]	[La/Fe]
FLD-121_100330	-0.99 ± 0.07	-0.07 ± 0.06	$+0.46 \pm 0.21$	$+0.56 \pm 0.07$
FLD-121_100514	-0.75 ± 0.07	-0.56 ± 0.06	-0.18 ± 0.15	-0.04 ± 0.06
FLD-121_100683	-0.77 ± 0.07	-0.35 ± 0.06	-0.16 ± 0.16	$+0.10 \pm 0.07$
FLD-121_100767	-0.88 ± 0.07	-0.65 ± 0.07	-0.08 ± 0.16	-0.33 ± 0.11
FLD-121_100781	-0.84 ± 0.07	-0.49 ± 0.06	$+0.03 \pm 0.16$	$+0.03 \pm 0.07$
FLD-121_100823	-0.53 ± 0.08	-0.29 ± 0.12	-0.26 ± 0.18	$+0.34 \pm 0.11$
FLD-419_1355	-1.14 ± 0.07	-0.73 ± 0.08	-0.35 ± 0.16	-0.44 ± 0.08
BD06448 (MW)	-0.64 ± 0.07	-0.03 ± 0.05	$+0.17 \pm 0.16$	$+0.22 \pm 0.07$

Table 4.4: [Cu/Fe], [Y/Fe], [Ba/Fe] and [La/Fe] abundances of SMC and MW targets of our study.

Target	[Nd/Fe]	[Eu/Fe]
FLD-121_100330	$+0.55 \pm 0.07$	$+1.05 \pm 0.07$
FLD-121_100514	-0.08 ± 0.08	$+0.68 \pm 0.07$
FLD-121_100683	-0.03 ± 0.07	$+0.62 \pm 0.07$
FLD-121_100767	-0.25 ± 0.07	$+0.27 \pm 0.07$
FLD-121_100781	-0.04 ± 0.07	$+0.48 \pm 0.07$
FLD-121_100823	$+0.34 \pm 0.11$	$+0.75 \pm 0.10$
FLD-419_1355	-0.40 ± 0.17	$< +0.10$
BD06448 (MW)	$+0.21 \pm 0.06$	$+0.42 \pm 0.07$

Table 4.5: [Nd/Fe] and [Eu/Fe] abundances of SMC and MW targets of our study. The abundances reported without errors and with the < sign are upper limit estimates.

Chapter 5

Comparison with previous works

In this chapter we compare our results with the available chemical abundances from Mucciarelli et al. (2023a), from whose work the sample of our metal-poor candidates was derived, and with the chemical abundances from Reggiani et al. (2021), since their four metal-poor SMC stars are in common with our sample.

5.1 Reggiani et al. (2021)

Finally, we provide a comparison between our analysis from UVES spectra and the analysis by Reggiani et al. (2021) from Magellan MIKE spectra. We recall that this MIKE dataset has lower SNR and resolution with respect to the UVES one. For each star of our sample that was analysed by Reggiani et al. (2021), i.e. FLD-121_100330, FLD-121_100514, FLD-121_100683 and FLD-121_100781, we computed, for each element available in both analyses, the difference between the measured abundances and summed in quadrature their errors. The differences were then computed for: iron, the light element Na, the α -elements Mg, Si, Ca, the iron-peak elements Mn and Ni and the s -process element Ba for all the four stars mentioned above; the s -process element Cu for FLD-121_100683 and FLD-121_100781; the s -process element Nd for FLD-121_100330, FLD-121_100514 and FLD-121_100781; the r -process element Eu for FLD-121_100330 and FLD-121_100781. The differences between the $[X/Fe]$ abundances ($[Fe/H]$ abundances in the case of iron) for each star are visualized in Figure 5.1.

The average difference in $[Fe/H]$ between UVES and MIKE analysis is $+0.28 \pm 0.06$, reaching $+0.44$ dex for the star FLD-121_100514. The systematically lower $[Fe/H]$ obtained by Reggiani et al. (2021) are likely ascribable to the differences in stellar parameters (see Section 3.1) and in particular the lower T_{eff} and higher v_t . As already discussed, the use of a spectroscopic determination of all the parameters, coupled with the low quality of the used spectra (introducing a bias against the weak lines) leads to lower T_{eff} and higher v_t .

The comparison of the other elemental abundances delineate a quite variable pattern: while two stars (FLD-121_100330 and FLD-121_100683) generally exhibit elemental abundances compatible with Reggiani et al. (2021) analysis, within a 2σ level, the other two (FLD-121_100514 and FLD-121_100781) are characterised by systematically lower abundances, not compatible with Reggiani et al. (2021) analysis.

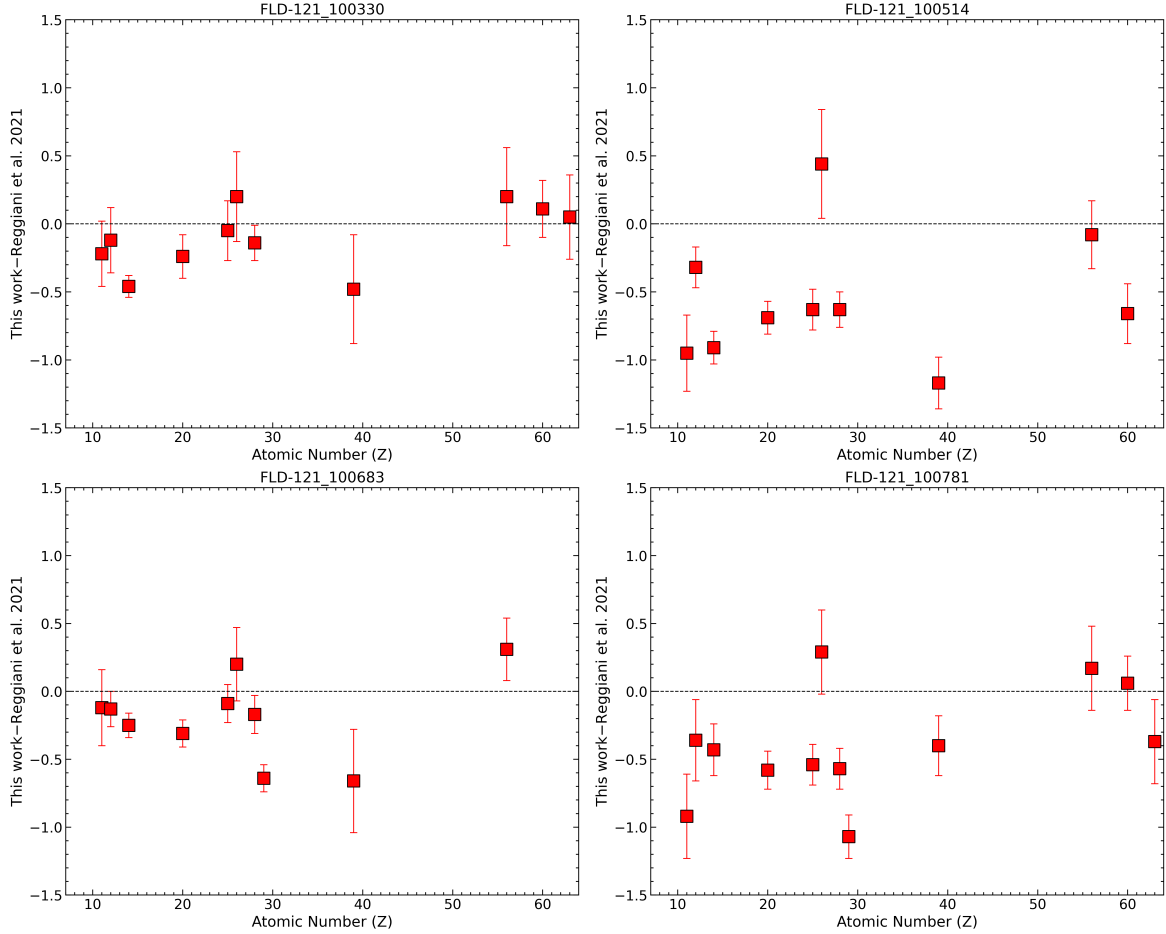


Figure 5.1: Differences between $[X/Fe]$ abundances ($[Fe/H]$ abundances in the case of iron) from our analysis and Reggiani et al. (2021) analysis as a function of the atomic number. Errorbars are the quadrature sum of the errors to the abundance measurements from the two analyses.

Several factors led to the observed discrepancies in the four stars studied through both UVES and Magellan MIKE spectra and discussed above. The choice of different sets of stellar parameters (T_{eff} , $\log g$, v_t) is surely responsible for some discrepancies in the final abundances. We remark that the highly significant offset between the microturbulence values we retrieved from Mucciarelli et al. (2023a) and the ones adopted by Reggiani et

al. (2021), and previously discussed in 3.1: Reggiani et al. (2021) v_t values, obtained by means of a spectroscopic approach, are computed with few small potential Fe I lines, leading to fairly too high microturbulences, which are typically observed in supergiants, rather than in giant stars. Significant differences in microturbulence definitely have an impact on the final abundance measurements.

On top of the discrepancies in atmospheric parameters, the use of different linelists and the different characteristics of the available spectra constitute the other main reason for the observed differences between the two sets of elemental abundances. The MIKE echelle spectrograph guarantees a wavelength coverage comparable with that of UVES spectra, while the adopted spectral resolution in the Reggiani et al. (2021) sample is about 20,000, significantly lower than the UVES one. Moreover, the larger exposure time each of the targets have been addressed in the UVES observations analysed in this work provides a higher SNR throughout the UVES spectra with respect to the MIKE observations by Reggiani et al. (2021). This fact consequently makes possible to identify less intense absorption features, and a larger number of absorption lines is identified overall. The availability of different sets of absorption features for each element is certainly having a key role in causing the significant abundance discrepancies discussed above.

5.2 Mucciarelli et al. (2023a)

We provide a comparison between the abundances measured from UVES spectra of our targets and the abundances measured from GIRAFFE spectra in Mucciarelli et al. (2023a) for the same sample of SMC stars. For each star of our sample, we computed, for each element available in both analyses, the difference between the measured abundances (or between the measured abundance and the upper limit) and summed in quadrature their errors (or simply used the only error available when comparing with an upper limit). The abundance differences were then computed for: iron, the light element Na, all the previously discussed α -elements, the iron-peak elements V and Ni and the s -process elements Cu, Ba and La. The sets of differences between the averages of $[X/Fe]$ abundances ($[Fe/H]$ abundances in the case of iron) for each of our targets are shown in Figures 5.2.

The iron abundances from UVES analysis are all compatible, within 1σ with the GIRAFFE iron abundances from Mucciarelli et al. (2023a), confirming the metal-poor nature of those stars as deduced from the medium resolution GIRAFFE observations. The only, yet marginal, exception is represented by the target FLD-121_100823, whose iron abundance is 0.29 dex (1.8σ) higher than the value from GIRAFFE, probably due to the low SNR of the GIRAFFE spectra used for this target (see Mucciarelli et al. 2023a).

The abundances we measured in all stars, except FLD-121_100823, for the other elements are compatible with the ones from GIRAFFE analysis within the 2σ level. The

only element displaying a significant difference between the two analyses is vanadium, which is significantly lower (-0.37 ± 0.07) with respect to the previous GIRAFFE analysis of the same targets. The reason for this discrepancy resides in the small number of mainly weak lines available in GIRAFFE spectra; UVES spectra are conversely covering a larger number of stronger absorption lines.

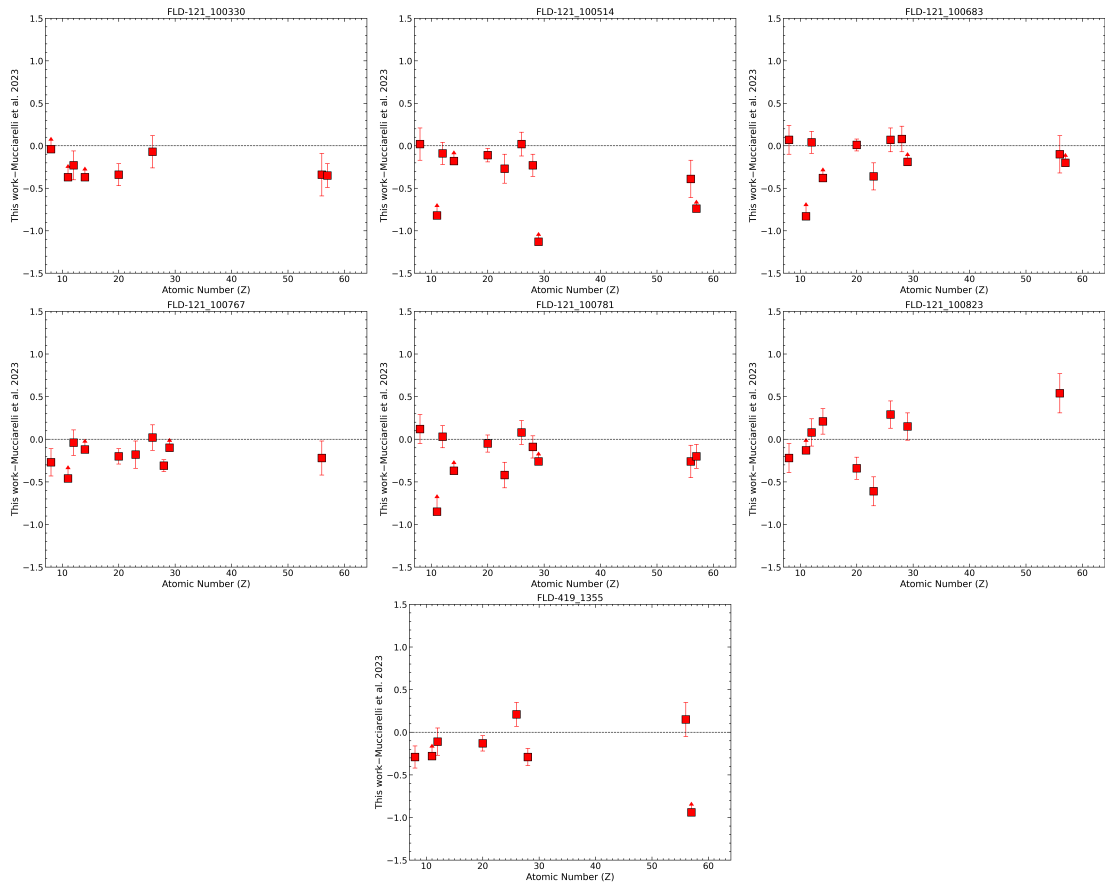


Figure 5.2: Differences between $[X/Fe]$ abundances ($[Fe/H]$ abundances in the case of iron) from our analysis and Mucciarelli et al. (2023a) analysis as a function of the atomic number. Errorbars are the quadrature sum of the errors to the abundance measurements from the two analyses.

Chapter 6

Conclusions

We analysed wide coverage, high resolution ($R \sim 40,000$) and high SNR (~ 60) UVES spectra for seven metal-poor RGB SMC stars, previously analysed using GIRAFFE spectra ($R \sim 20,000$) with low SNR (~ 30). This new dataset allows to determine precise chemical abundance for a large number of key elements. In particular, with respect to the previous analysis, some important new elements (i.e. Mn, Zn, Eu) have been measured. Also, we applied NLTE corrections for several species, using the most updated grids of NLTE corrections. We note that NLTE corrections have been applied only to Na abundances in previous works on metal-poor SMC stars.

The main results emerging from this chemical analysis are summarised hereafter:

- We confirm that all the stars are metal-poor, and all but one in the range of $[\text{Fe}/\text{H}]$ between -2.1 and -1.7 dex and likely corresponding to the first Gyr of the SMC life.
- metal-poor SMC stars show lower sodium abundances than Galactic stars in the early phases of SMC chemical enrichment; this discrepancy has been previously observed at higher $[\text{Fe}/\text{H}]$ as well: low $[\text{Na}/\text{Fe}]$ in SMC stars may confirm massive stars and CC SNe provide a lower contribution to the chemical enrichment of the SMC in its early epochs;
- α -elements are, as expected, enhanced in metal-poor SMC stars, but at a lower level with respect to MW stars of similar $[\text{Fe}/\text{H}]$. This lower $[\alpha/\text{Fe}]$ enhancement and a mild decrease of $[\alpha/\text{Fe}]$ for increasing metallicity are consistent with the SFR of the SMC, slower than that of the MW. This dataset suggests that the α -knee occurs at lower $[\text{Fe}/\text{H}]$ than in the MW, but it is not yet possible to properly identify it. This is summarised in Fig. 6.1 that shows the fun with $[\text{Fe}/\text{H}]$ of hydrostatic (Mg and O) and explosive (Si and Ca) α -elements. Six stars draw a decreasing trend reaching solar or mildly enhanced $[\alpha/\text{Fe}]$, while the most metal-rich star of the sample results to be enhanced in $[\alpha/\text{Fe}]$;

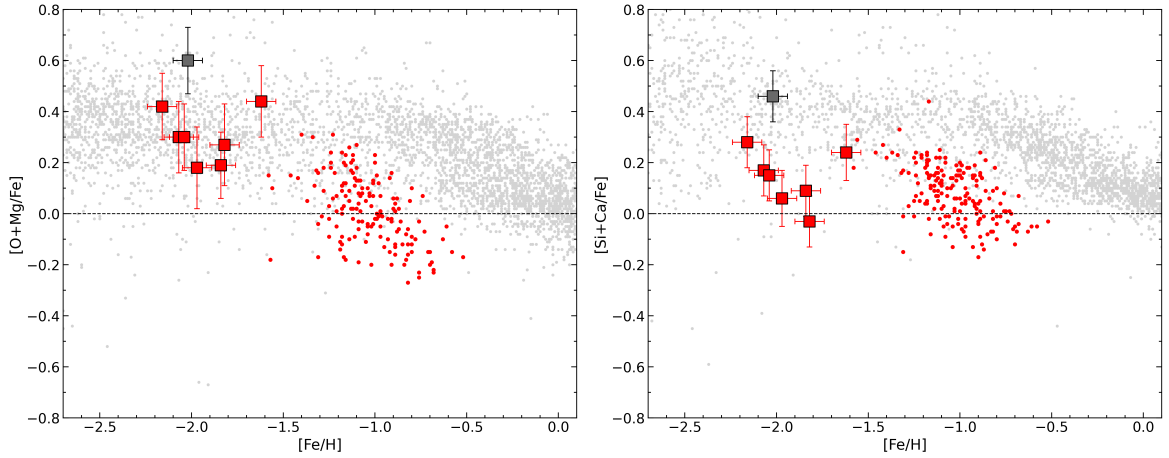


Figure 6.1: Hydrostatic (Mg and O) and explosive (Si and Ca) $[\alpha/\text{Fe}]$ abundances as function of $[\text{Fe}/\text{H}]$ for the analysed SMC (red squares) and MW (grey square) targets. $[\alpha/\text{Fe}]$ abundances for MW stars from SAGA database (grey points) in the range $-2.7 < [\text{Fe}/\text{H}] < +0.1$ are shown for comparison.

- $[\text{Zn}/\text{Fe}]$ is generally subsolar and lower than in Galactic stars, which suggests a lower contribution by HNe and therefore by very massive stars ($> 30 - 35 M_{\odot}$). This is compatible with the low SFR of the SMC, reducing the contribution by very massive stars;
- the SMC is characterised by a large star-to-star scatter for $[\text{Eu}/\text{Fe}]$, similar to that observed in metal-poor MW stars. This indicates that the r -processes are efficient in the SMC but affected by the stochastic nature of the main sites of production (i.e. neutron star mergers);
- also the s -process elements show large star-to-star scatter not compatible within the uncertainties. At these metallicities, the production of these elements is driven by r -processes. Fig. 6.2 shows the run of $[s/\text{Eu}]$ with $[\text{Fe}/\text{H}]$. Almost all the stars have subsolar values. The nucleosynthesis of the heavy elements has been dominated by the r -process, both because this type of process seems to be very efficient in the SMC and because the AGB stars have had no time to evolve and leave their chemical signatures in the interstellar medium. The only stars with high $[s/\text{Eu}]$ is also the most r -rich star of the sample;
- summarizing, the SMC metal-poor stars display distinct abundances with respect to the MW stars. In particular, the abundance ratios of elements produced by massive stars are lower than those measured in the MW stars. This suggests that the gas from which these stars formed was poorly enriched by the most massive stars. This can be explained in light of the low SF rate expected for a galaxy as

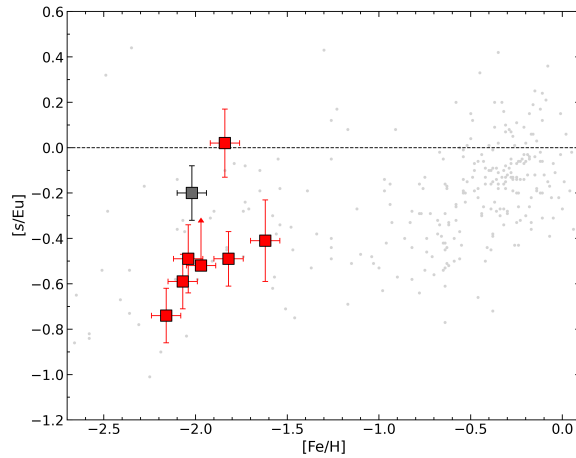


Figure 6.2: $[s/\text{Eu}]$ abundances as function of $[\text{Fe}/\text{H}]$ for the analysed SMC (red squares) and MW (grey square) targets. $[s/\text{Eu}]$ abundances for MW stars from Venn et al. (2004, grey points) in the range $-2.7 < [\text{Fe}/\text{H}] < +0.1$ are shown for comparison.

small as the SMC, leading to a lower contribution by massive stars to the overall chemical enrichment of the galaxy (Jeřábková et al. 2018; Yan et al. 2020).

High resolution spectroscopy of metal-poor stars of MCs and of other MW satellites permits to better understand the early chemical enrichment of such systems, highlighting the similarities and differences with our Galaxy, both in terms of stellar content and galactic environment influence on SF processes. The analysis of high-resolution UVES spectra for the seven metal-poor SMC stars of this work confirms there are differences between the MCs and MW chemical enrichment histories, and also adds new pieces of information about the knowledge of the first SMC stellar generations. This work demonstrates the need to observe metal-poor stars in external galaxies using high-quality spectroscopic dataset and in particular the importance to measure some chemical elements (i.e. Zn, Eu) that provide crucial insights to the chemical enrichment by HNe and neutron star mergers.

Bibliography

- [1] Alexeeva, S. A., Pakhomov, Yu. V., Mashonkina, L. I. 2014, [AstL](#), 40, 406
- [2] Andrae, R., Fouesneau, M., Creevey, O., Ordenovic, C., et al. 2018, [A&A](#), 616, A8
- [3] Asplund, M. 2005, [ARA&A](#), 43, 481
- [4] Bekki, K., & Chiba, M. 2005, [MNRAS](#), 356, 680
- [5] Besla, G. 2015, ArXiv eprints, arXiv:[1511.03346]
- [6] Besla, G., Kallivayalil, N., Hernquist, L., Robertson, B., et al. 2007, [ApJ](#), 668, 949
- [7] Besla, G., Kallivayalil, N., Hernquist, L., et al. 2010, [ApJ](#), 721, 97
- [8] Brocato, E., Castellani, V., Ferraro, F. R., et al. 1996, [MNRAS](#), 282, 614
- [9] Cacciari, C., & Freeman, K. C. 1983, [ApJ](#), 268, 185
- [10] Cacciari, C., Bragaglia, A., Rossetti, E., Fusi Pecci, F., et al. 2004, [A&A](#), 413, 343
- [11] Caffau, E., Ludwig, H.-G., Steffen, M., Freytag, B., et al. 2011, [SoPh](#), 268, 255
- [12] Carrera, R., Gallart, C., Aparicio, A., Costa, E., et al. 2008, [AJ](#), 136, 1039
- [13] Castelli, F., & Kurucz, R. L. 2003, [IAU Symp.](#), 210, poster A20
- [14] Chiti, A., Frebel, A., Jerjen, H., Kim, D., Norris, J. E. 2020, [ApJ](#), 891, 8
- [15] Chiti, A., Mardini, M., Limberg, G., Frebel, A., et al. 2024, [Nat. Astron.](#), 8, 637
- [16] Cignoni, M., Cole, A. A., Tosi, M., Gallagher, J. S., et al. 2012, [ApJ](#), 754, 130
- [17] Cignoni, M., Cole, A. A., Tosi, M., Gallagher, J. S., et al. 2013, [ApJ](#), 775, 83
- [18] Clayton, D., [Handbook of Isotopes in the Cosmos](#), Cambridge University Press, 2003

- [19] Dekker, H., D’Odorico, S., Kaufer, A., Delabre, B., et al. 2000, [SPIE](#), 4008, 534
- [20] Dobbie, P. D., Cole, A. A., Subramaniam, A., Keller, S. 2014a, [MNRAS](#), 442, 1663
- [21] Dobbie, P. D., Cole, A. A., Subramaniam, A., Keller, S. 2014b, [MNRAS](#), 442, 1680
- [22] Frebel, A., & Norris, J. E. 2015, [ARA&A](#), 53, 631
- [23] Frebel, A., Casey, A. R., Jacobson, H. R., Yu, Q. 2013, [ApJ](#), 769, 57
- [24] Frebel, A., Norris, J. E., Gilmore, G., Wyse, R. F. G. 2016, [ApJ](#), 826, 110
- [25] Gaia Collaboration (Babusiaux, C., et al.) 2018, [A&A](#), 616, A10
- [26] Gaia Collaboration (Brown, A. G. A., et al.) 2021, [A&A](#), 649, A1
- [27] Glatt, K., Gallagher, J. S., Grebel, E. K., Nota, A., et al. 2008, [AJ](#), 135, 1106
- [28] Graczyk, D., Pietrzynski, G., Thompson, I. B., et al. 2014, [ApJ](#), 780, 59
- [29] Gratton, R. G., Pilachowski, C. A., Sneden, C. 1984, [A&A](#), 132, 11
- [30] Gratton, R. G., Sneden, C., Carretta, E., Bragaglia, A. 2000, [A&A](#), 354, 169
- [31] Grevesse, N., & Sauval, A. J. 1998, [SSR](#), 85, 161
- [32] Harris, J., Zaritsky, D. 2004, [AJ](#), 127, 1531
- [33] Jeřábková, T., Hasani Zonoozi, A., Kroupa, P., et al. 2018, [A&A](#), 620, A39
- [34] Johnson, J. A., Ivans, I. I., Stetson, P. B. 2006, [ApJ](#), 640, 801
- [35] Kallivayalil, N., van der Marel, R. P., Besla, G., et al. 2013, [ApJ](#), 764, 161
- [36] Kobayashi, C., Karakas, A. I., Lugaro, M. 2020, [ApJ](#), 900, 179
- [37] Krauss, L. M., & Chaboyer, B. 2003, [Science](#), 299, 65
- [38] Kurucz, R. L. 2005, [MSAIS](#), 8, 14
- [39] Lallement, R., Vergely, J. L., Babusiaux, C., Cox, N. L. J. 2022, [A&A](#), 661, A147
- [40] Lapenna, E., Mucciarelli, A., Origlia, L., Ferraro, F. R. 2012, [ApJ](#), 761, 33
- [41] Lattimer, J. M., & Schramm, D. N. 1974, [ApJ](#), 192, L145
- [42] Mallia, E. A., & Pagel, B. E. J., [MNRAS](#), 194, 421
- [43] Mashonkina, L. 2013, [A&A](#), 550, A28

- [44] Mashonkina, L., & Gehren, T. 2000, [A&A](#), 364, 249
- [45] Mashonkina, L., Gehren, T., Shi, J.-R., Korn, A. J., et al. 2011, [A&A](#), 528, A87
- [46] Mashonkina, L. I., Belyaev, A. K. 2019, [AstL](#), 45, 341
- [47] Mashonkina, L., Pakhomov, Y., Sitnova, T., et al. 2023, [MNRAS](#), 524, 3526
- [48] Massana, P., Ruiz-Lara, T., Noël, N. E. D., et al. 2022, [MNRAS](#), 513, L40
- [49] Matteucci, F., & Greggio, L. 1986, [A&A](#), 154, 279
- [50] Meszaros, Sz., Dupree, A. K., Szentgyorgyi, A. 2008, [AJ](#), 135, 1117
- [51] Molero, M., Simonetti, P., Matteucci, F., della Valle, M. 2021, [MNRAS](#), 500, 1071
- [52] Mucciarelli, A. 2014, [AN](#), 335, 79
- [53] Mucciarelli, A., & Bonifacio, P. 2020, [A&A](#), 640, A87
- [54] Mucciarelli, A., Carretta, E., Origlia, L., Ferraro, F. R. 2008, [AJ](#), 136, 375
- [55] Mucciarelli, A., Origlia, L., Ferraro, F. R. 2010, [ApJ](#), 717, 277
- [56] Mucciarelli, A., Pancino, E., Lovisi, L., Ferraro, F. R., et al. 2013, [ApJ](#), 766, 78
- [57] Mucciarelli, A., Bellazzini, M., Massari, D. 2021a, [A&A](#), 653, A90
- [58] Mucciarelli, A., Massari, D., Minelli, A., et al. 2021b, [Nat. Astron.](#), 5, 1247
- [59] Mucciarelli, A., Minelli, A., Bellazzini, M., Lardo, C., et al. 2023a, [A&A](#), 671, A124
- [60] Mucciarelli, A., Minelli, A., Lardo, C., Massari, D., et al. 2023b, [A&A](#), 677, A61
- [61] Nidever, D. L., Hasselquist, S., Hayes, C. R., Hawkins, K., et al. 2020, [ApJ](#), 895, 88
- [62] Nishimura, N., Takiwaki, T., Thielemann, F.-K. 2015, [ApJ](#), 810, 109
- [63] Noël, N. E. D., Gallart, C., Costa, E., Méndez, R. A. 2007, [AJ](#), 133, 2037
- [64] Olsen, K. A. G., Hodge, P. W., Mateo, M., et al. 1998, [MNRAS](#), 300, 665
- [65] Pagel, B. E. J., & Tautvaisiene, G. 1998, [MNRAS](#), 299, 535
- [66] Parisi, M. C., Geisler, D., Carraro, G., Clariá, J. J., et al. 2016, [AJ](#), 152, 58
- [67] Pompeia, L., Hill, V., Spite, M., Cole, A., Primas, F., et al. 2008, [A&A](#), 480, 379
- [68] Reggiani, H., Schlaufman, K. C., Casey, A. R., et al. 2021, [AJ](#), 162, 229

- [69] Ripepi, V., Cioni, M.-R. L., Moretti, M. I., et al. 2017, [MNRAS](#), 472, 808
- [70] Romano, D., & Matteucci, F. 2007, [MNRAS](#), 378, L59
- [71] Romano, D., Karakas, A. I., Tosi, M., Matteucci, F. 2010, [A&A](#), 522, A32
- [72] Rubele, S., Pastorelli, G., Girardi, L., et al. 2018, [MNRAS](#), 478, 5017
- [73] Ruiz-Lara, T., Gallart, C., Monelli, M., Nidever, D., et al. 2020 [A&A](#), 639, L3
- [74] Sbordone, L., Bonifacio, P., Castelli, F., Kurucz, R. L. 2004, [MSAIS](#), 5, 93
- [75] Schlafly, E. F., & Finkbeiner, D. P. 2011, [ApJ](#), 737, 103
- [76] Schlaufman, K. C., & Casey, Andrew R. 2014, [ApJ](#), 797, 13
- [77] Siegel, D. M., Barnes, J., Metzger, B. D. 2019, [Nature](#), 569, 241
- [78] Simon, J., Fu, S. W., Geha, M., Kelson, D. D., et al. 2019, [AAS](#), 233, 449.04
- [79] Sitnova, T. M., Yakovleva, S. A., Belyaev, A. K., et al. 2022, [MNRAS](#), 515, 1510
- [80] Skrutskie, M. F., Cutri, R. M., Stiening, R., et al. 2006, [AJ](#), 131, 1163
- [81] Stetson, P. B., & Pancino, E. 2008, [PASP](#), 120, 1332
- [82] Suda, T., Katsuta, Y., Yamada, S., Suwa, T., et al. 2008, [PASJ](#), 60, 1159
- [83] Tafelmeyer, M., Jablonka, P., Hill, V., Shetrone, M., et al. 2010, [A&A](#), 524, A58
- [84] Tinsley, B. M. 1979, [ApJ](#), 229, 1046
- [85] Tinsley, B. M. 1980, [FCPh](#), 5, 287
- [86] Tolstoy, E., Hill, V., & Tosi, M. 2009, [ARA&A](#), 47, 371
- [87] Tonry, J., & Davis, M. 1979, [AJ](#), 84, 1511
- [88] Van der Swaelmen, M., Hill, V., Primas, F., Cole, A. A. 2013, [A&A](#), 560, A44
- [89] Venn, K. A., Irwin, M., Shetrone, M. D., Tout, C. A., et al. 2004, [AJ](#), 128, 1177
- [90] Wagner-Kaiser, R., Mackey, D., Sarajedini, A., et al. 2017, [MNRAS](#), 471, 3347
- [91] Yan, Z., Jeřábková, T., Kroupa, P. 2020, [A&A](#), 637, A68

